

Article

# Numerical Investigation on the Evolution Process of Different Vortex Structures and Distributed Blowing Control for Dynamic Stall Suppression of Rotor Airfoils

Guoqiang Li <sup>1,2</sup> , Shihe Yi <sup>1</sup>, Binbin Li <sup>3,\*</sup> and Xin Zhang <sup>2</sup>

<sup>1</sup> College of Aerospace Science and Engineering, National University of Defense Technology, Changsha 410000, China; cardcl@126.com (G.L.); yishihe@nudt.edu.cn (S.Y.)

<sup>2</sup> Low Speed Aerodynamics Institute, China Aerodynamics Research and Development Center, Mianyang 621000, China; lookzx@mail.ustc.edu.cn

<sup>3</sup> School of Civil Engineering and Architecture, Southwest University of Science and Technology, Mianyang 621000, China

\* Correspondence: libinbin-8@163.com

**Abstract:** The influencing characteristic for the evolution mechanism of a dynamic stall vortex structure and distributed blowing control on rotor airfoils was investigated. Based on the moving-embedded grid method, the finite volume scheme, and Roe's FDS scheme, a simulation method for the unsteady flow field of a pitch-oscillating airfoil was established. The flow field of the NACA63-218 airfoil was calculated using Reynolds-averaged Navier–Stokes equations. The evolution processes of different vortex structures during dynamic stall and the principal controlled vortex mechanism affecting aerodynamic nonlinearity were analyzed based on the pressure contours  $C_p$  and  $Q$  of the flow field structure and the spatiotemporal evolution characteristics of the wall pressure distribution. The research indicated that dynamic stall vortices (DSVs) and shear layer vortices (SLVs) were the major sources of the increase in aerodynamic coefficients and the onset of nonlinear hysteresis. Building upon these findings, the concept of distributed blowing control for DSVs and shear layer vortices (SLVs) was introduced. A comparative analysis was conducted to assess the control effectiveness of dynamic stall with different blowing locations and blowing coefficients. The results indicated that distributed blowing control effectively inhibited the formation of DSVs and reduced the intensity of SLVs. This led to a significant decrease in the peak values of the drag and pitch moment coefficients and the disappearance of secondary peaks in the aerodynamic coefficients. Furthermore, an optimal blowing coefficient existed. When the suction coefficient  $C_{\mu}$  exceeded 0.03, the effectiveness of the blowing control no longer showed a significant improvement. Finally, with a specific focus on the crucial motion parameters in dynamic stall, the characteristics of dynamic stall controlled by air blowing were investigated. The results showed that distributed air blowing control significantly reduced the peak pitching moment coefficient and drag coefficient. The peak pitching moment coefficient was reduced by 72%, the peak drag coefficient was reduced by 70%, and the lift coefficient hysteresis loop area decreased by 46%. Distributed blowing jet control effectively suppressed the dynamic stall characteristics of the airfoil, making the unsteady load changes gentler.

**Keywords:** rotor airfoil; dynamic stall vortex; evolutionary process; distributed blowing; flow control



**Citation:** Li, G.; Yi, S.; Li, B.; Zhang, X. Numerical Investigation on the Evolution Process of Different Vortex Structures and Distributed Blowing Control for Dynamic Stall Suppression of Rotor Airfoils. *Actuators* **2024**, *13*, 30. <https://doi.org/10.3390/act13010030>

Academic Editor: Luigi de Luca

Received: 26 November 2023

Revised: 7 January 2024

Accepted: 9 January 2024

Published: 11 January 2024



**Copyright:** © 2024 by the authors. Licensee MDPI, Basel, Switzerland. This article is an open access article distributed under the terms and conditions of the Creative Commons Attribution (CC BY) license (<https://creativecommons.org/licenses/by/4.0/>).

## 1. Introduction

The dynamic stall of an airfoil refers to the strong unsteady and nonlinear flow phenomenon caused by lifting components such as the wing or rotor blade when the angle of attack undergoes periodic or abrupt dynamic changes; this leads to widespread airflow separation above the airfoil surface [1,2]. The forward flight speed, noise, and vibration levels of a helicopter are greatly affected by the dynamic stall characteristics of the airfoil of the helicopter rotor [3]. Dynamic stall leads to aerodynamic issues in the helicopter

rotor, including an increase in the required power, a sudden drop in lift, reverse torque, and a sudden increase in blade vibrations, which limits the helicopter's flight speed and maneuverability. These serve as the primary factors restricting the improvement of the aerodynamic performance in helicopter rotors [4]. Therefore, research on the dynamic stall characteristics of a rotor airfoil to reveal the evolution process of dynamic stall has had a guiding role in improving the aerodynamic performance of rotors and improving the overall performance of helicopters. It had always been a research hotspot and cutting-edge issue in relation to the unsteady aerodynamics of helicopter rotors [5,6].

The mechanism of dynamic stall on a helicopter rotor airfoil is intricate, and its suppression poses significant challenges, making it a focal point of attention in the field of helicopter aerodynamics. In the 1940s, Himmelskamp [7] first observed the phenomenon of dynamic stall in experiments. However, due to the relatively low demands for aircraft maneuverability at the time and limited analytical methods, this phenomenon was not extensively investigated. It was not until the 1960s, following a helicopter rotor experiment, that dynamic stall garnered widespread attention, initiating subsequent research on this phenomenon. Ham [8] was among the first to provide a theoretical description of the development process of dynamic stall. From the 1970s onward, McCroskey et al. [9] conducted a substantial number of experimental studies on the dynamic stall phenomenon, contributing to a deeper understanding of the formation mechanism of dynamic stall. Carr, L.W. [10,11] delineated that the fundamental characteristics of dynamic stall encompass the presence of intricate unsteady separation and large-scale vortex structures in the flow field, resulting in the manifestation of pronounced nonlinear hysteresis properties in aerodynamics. Geissler et al. [12] conducted experimental and numerical studies on the dynamic stall characteristics on the OA312 airfoil and found that the development, shedding, and accumulation of leading-edge vorticity had an important impact on the dynamic stall characteristics of the airfoil. Wang et al. [13] employed particle image velocimetry (PIV) technology to measure the transport velocity of leading-edge vortices on OA209 and SC1095 airfoils. The study indicated that the transport velocity of leading-edge vortices was primarily influenced by the oscillation frequency of the airfoil. As the oscillation frequency increases, the transport velocity of the leading-edge vortices is also promoted accordingly. Ekaterinaris et al. [14] conducted a thorough summary of the numerical methods and research outcomes employed in the study of airfoils' dynamic stall. The results indicated that factors such as the reduced frequency, amplitude angle, average angle of attack, pivot location, and free-stream Mach number during airfoil pitching motion had a direct impact on the strength, development, and shedding of the dynamic stall vortices. Additionally, the geometric shape of the airfoil also influenced the dynamic stall characteristics of the airfoil. Naughton et al. [15] used PIV phase-locked averaging technology and surface pressure testing technology to measure the unsteady aerodynamic characteristics of wind turbine airfoils under dynamic stall. Analysis of the measurement results showed that there were four stall types: (1) trailing-edge stall; (2) trailing-edge stall with a secondary vortex; (3) trailing-edge stall with a separated vortex; and (4) the stall induced by a leading-edge separated vortex. Airfoil dynamic stall is a very complex process, including the formation and evolution of different vortex structures. Ullah et al. [16] conducted a study of dynamic stall on pitching swept finite-aspect-ratio wings using lifetime PSP. Gardner, A.D. et al. [17] undertook an investigation of the three-dimensional dynamic stall on an airfoil using fast-response pressure-sensitive paint. Disotell, K.J. et al. [18] conducted a study on global surface pressure measurements of the static and dynamic stall on a wind turbine airfoil at a low Reynolds number. Due to the complexity and high cost of wind tunnel experiments on airfoil dynamic stall and the limitations imposed by the measurement equipment and technology, research has been typically confined to limited operating conditions. With the advancement in computational fluid dynamics, numerical simulation gradually became a crucial approach to studying the dynamic stall characteristics of airfoils [19–25]. Visbal and Garmann [26–29] studied the effect of sweep and unsweep on the dynamic stall of

a pitching finite-aspect-ratio wing and undertook an analysis of the dynamic stall on a pitching airfoil using high-fidelity large-eddy simulations.

Many scholars, both domestically and internationally, have conducted extensive numerical simulations and experimental research on the flow control of rotor airfoil dynamic stall, achieving significant breakthroughs. Flow control can be categorized into passive control and active control based on whether external energy injection is required. Passive flow control methods include leading-edge deformation [30–33], a waveform leading edge [34], trailing-edge deflection flaps [35–37], Gurney flaps [38–40], and vortex generators [41,42], among others. These methods primarily control dynamic stall through two pathways: (1) shape deformation, causing changes in the wing surface pressure distribution; and (2) altering the flow state over the wing surface to inhibit the formation and development of dynamic stall vortices. While these control methods performed well on fixed wings, they were less practical on helicopter rotors. On the one hand, this was because they faced a rapidly changing working environment, where passive control struggled to consistently maintain high control efficiency. The active flow control methods included air blowing control [43–47], a synthetic jet [48], and plasma control technology [49–54], among others. The blowing control technology involved injecting high-momentum gas into the boundary layer to reduce the flow instability [55], suppress flow separation, and consequently delay dynamic stall. Plasma and synthetic jet control have simple structures and small volumes, but inhibiting the dynamic stall vortices of airfoils under high Mach numbers and extreme conditions is challenging. Implementing continuous and efficient control is difficult. Air blowing control, on the other hand, is a widely researched solution with advantages such as high intensity and high maturity. Using a high-speed airstream to inject energy into the flow field near the airfoil controls the generation of dynamic stall vortices without introducing additional “waste drag”. Adjusting the opening and closing of the blowing not only effectively controls the retreating blades of the rotor [56,57] but also does not interfere with the advancing blades. It is expected to be a promising technical means to solve the dynamic stall problem of airfoils and rotor blades.

Although there has been some research on blowing control of rotor airfoil dynamic stall, both domestically and internationally, the focus has mainly been on the study of the blowing airflow control methods. There has been a lack of research on the evolution processes of different vortex structures and the mechanisms of the main controlling vortices in rotor airfoil dynamic stall. Additionally, there is limited research on the blowing control of rotor airfoil dynamic stall under high wind speeds and high-frequency oscillations. This study establishes a numerical simulation method for the unsteady flow field of a pitching oscillation airfoil based on the overset grid technology, the finite volume method, and Roe’s FDS scheme. By solving the Reynolds-averaged Navier–Stokes equations, the flow field around the NACA63-218 airfoil under a high wind speed is simulated. Using an analysis of the spatiotemporal evolution characteristics of the flow structure and wall pressure distribution based on the pressure coefficient ( $C_p$ ) and Q contours, this study investigates the evolution processes of different vortex structures during dynamic stall and the main controlling vortex mechanism influencing the aerodynamic nonlinear hysteresis. This study aims to provide the necessary theoretical foundation for exploring more efficient and practical flow control methods and developing predictive methods for the evolution of dynamic stall. Building upon this, the concept of distributed blowing control is introduced, and the control effects of dynamic stall are compared for different blowing locations and blowing coefficients. Finally, focusing on the important motion parameters in airfoil dynamic stall, the control characteristics of distributed blowing control are studied under multiple operating conditions.

## 2. Geometric Model and Numerical Methods

### 2.1. Dynamic Chimera Grid System

The numerical model employed the NACA63-218 airfoil, as previously utilized in the XH-59A helicopter [58]. To simulate the unsteady aerodynamic characteristics during

airfoil pitching oscillation, dynamic chimera grid technology was used. This facilitated the movement of the airfoil grid and the exchange of information between the airfoil grid and the background grid. Figure 1 depicts a local view of the grid for the NACA63-218 airfoil. The grid exhibits the favorable characteristics of orthogonality and conformity to the airfoil geometry. The airfoil was subjected to a no-slip wall condition and the surrounding region of the background grid utilized a pressure far-field condition. The grid had 38,000 nodes for the airfoil and 68,000 nodes for the component. The  $y^+$  value was about 1 for the first layer of the grid, and the normal grid spacing near the wall increased outward at a rate of 1.2. The chord length ( $c$ ) of the airfoil was 0.35 m (consistent with the chord length dimension of the wind tunnel test model), the inflow velocity was  $M = 0.3$ , and the Reynolds number, based on the chord length, was  $Re = 2.41 \times 10^6$ . The atmospheric pressure was 101,325 Pa and the ambient temperature was  $T = 288.15$  K. In this case, the computational domain is depicted in Figure 2.

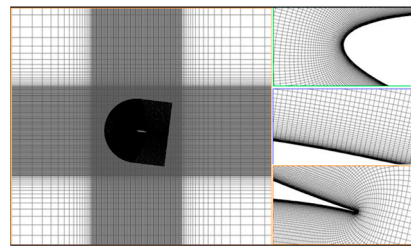


**Figure 1.** C-type grid around NACA63-218 airfoil.

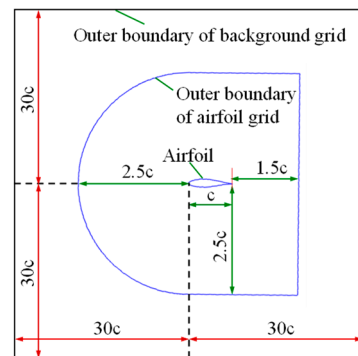


**Figure 2.** Schematic diagram of computational domain.

## 2.2. Governing Equations and Numerical Simulation Methods

To simulate the flow field around the rotor airfoil, unsteady Reynolds-averaged Navier–Stokes (RANS) equations are applied in this research, and the integral form of the governing equations is described as:

$$\frac{\partial}{\partial t} \int_{\Omega} W d\Omega + \oint_{\Omega} (F_c - F_v) dS = 0 \quad (1)$$

The conserved variable is  $W = [\rho \ \rho u \ \rho v \ \rho E]^T$ , where  $u$  and  $v$  are the Cartesian velocity components,  $\rho$  is the density, and  $E$  is the total energy per unit mass.  $\Omega$  is the control volume and  $S$  is the boundary of the control volume.  $F_c$  and  $F_v$  are the vectors of the convective fluxes and viscous fluxes, which are expressed as:

$$F_c = \begin{bmatrix} \rho V_r \\ \rho u V_r + n_x p \\ \rho v V_r + n_y p \\ \rho H V_r + V_t p \end{bmatrix}, \quad F_v = \begin{bmatrix} 0 \\ n_x \tau_{xx} + n_y \tau_{xy} \\ n_x \tau_{yx} + n_y \tau_{yy} \\ n_x \Theta_x + n_y \Theta_y \end{bmatrix} \quad (2)$$

where  $p$  is the pressure of the airflow and  $H$  is the total enthalpy per unit mass.  $V_r = V - V_t$ , where  $V$  is the velocity normal to the surface element  $dS$  and  $V_t$  is the contravariant velocity.  $n_x$  and  $n_y$  are the normal vector components of the control surface.  $\tau_{ij}$  is the viscous stress term and  $\Theta_i$  is the term used to describe the heat conduction in the fluid.

In this study, the highly accurate SST  $k-\omega$  turbulence model for capturing the flow separation phenomena was used. The discretization method utilized was the finite volume method, while pressure–density coupling was achieved using an implicit algorithm. The convective fluxes were discretized using the low-dissipation Roe’s FDS format, and the convective terms were discretized using a second-order upwind scheme. The time advancement scheme employed was a second-order implicit method. This study primarily investigated the dynamic stall control of an airfoil during pitch motion. The airfoil rotates about a pivot point located at  $0.25c$  along the chord, where  $c$  denotes the chord length. The airfoil undergoes forced pitching oscillation in a sinusoidal manner. The pitch motion was described by the following equation:

$$\alpha(t) = \alpha_0 + \alpha_m \sin(2kt) \quad (3)$$

In the given equation,  $\alpha_0$  represented the average angle of attack,  $\alpha_m$  was the amplitude of the angle of attack, and  $k$  was the reduction frequency, describing the extent of the unsteady effects of the oscillatory motion on the incoming flow. A higher value of  $k$  was a more significant unsteady effect. The expression for  $k$  could be formulated as follows:

$$k = \pi f c / V_\infty \quad (4)$$

Here,  $f$  was the oscillation frequency of the airfoil,  $c$  was the chord length of the airfoil, and  $V_\infty$  was the free-stream velocity.

### 2.3. Method Validation

Based on the dynamic chimera grid technology, the dynamic stall aerodynamic characteristics of the NACA63-218 airfoil were numerically validated using the computational fluid dynamics (CFD) method. Figure 3 presents a comparison between the calculated and experimental values of the dynamic aerodynamic coefficients for the airfoil. The conditions for both the calculations and experiments were as follows: the airfoil’s chord length was  $c = 0.35$  m, the free-stream Mach number was 0.1, the angle of attack followed the variation pattern  $\alpha = 14^\circ + 10^\circ \sin(2kt)$  with a reduction frequency of  $k = 0.097$ , and the Reynolds number was  $R_e = 7.0 \times 10^5$  (Due to limitations in the experimental setup and wind tunnel, the wind speed did not cover a higher range). The figure demonstrates the basic consistency between the numerical calculations and experimental results, particularly regarding the lift coefficient during the airfoil’s pitching-up phase and the simulation of an unsteady load during dynamic stall. These findings validated the effectiveness of the proposed numerical simulation method in accurately capturing the unsteady aerodynamic characteristics on the NACA63-218 airfoil under dynamic stall conditions. Although a wind tunnel test is a reliable means of obtaining airfoil aerodynamics data, the test model is surrounded by the wall of the tunnel, and the constraints of the wall will interfere with the flow and aerodynamic forces of the airfoil. Even though the study tries its best to minimize this interference, there will still be some impact, as shown in Figure 3. Considering that the main research object is the improvement of the dynamic stall characteristics of airfoils using a blowing jet, and the comparative analysis is on the difference in the performance changes in airfoils under aerodynamic actuation opening and closing conditions, it is reasonable to believe that the data analysis and conclusions obtained in this study are reliable. The dynamic stall flow studied is notoriously three-dimensional [59]; however, two-dimensional simulations can also accurately reflect the changes in aerodynamic curves during dynamic stall processes [60].

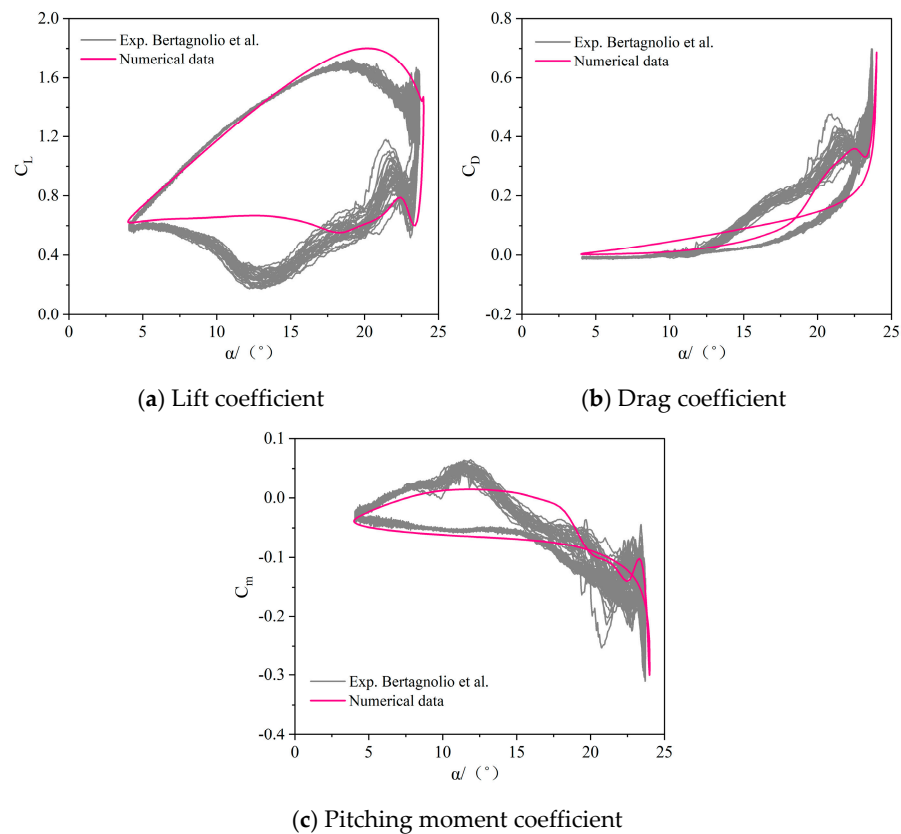


**Figure 3.** Comparison of calculated aerodynamic coefficients of airfoils with the literature [61].

### 3. Evolution Process of the Different Vortex Structures of Dynamic Stall and the Active Control Vortex Mechanism of Nonlinear Aerodynamics

#### 3.1. Analysis of the Aerodynamic Characteristics of Dynamic Stall

Numerical simulations were conducted to investigate the dynamic stall aerodynamic characteristics on the NACA63-218 airfoil. The computational conditions represented the typical operating state of a trailing-edge rotor blade:  $M = 0.3$ , the angle of attack varied according to  $\alpha = 12^\circ + 10^\circ \sin(2kt)$  with a reduction frequency of  $k = 0.129$ , and the Reynolds number was  $Re = 2.41 \times 10^6$ . To accurately simulate the unsteady aerodynamic forces during the dynamic stall of the airfoil, the oscillation period was divided into 600 time steps. Each sub-iteration consisted of 200 steps and the calculations were performed for two cycles. In Figure 4, the lift, drag, and moment coefficient curves of the airfoil are displayed, which were calculated using the SST  $k-\omega$  turbulence model. Figure 4 includes six different moments labeled A to F.

From the figure, the following can be observed: (1) The upstroke process: along point A to point B, the lift coefficient changed linearly with the angle of attack, the lift line slope  $C_L^\alpha$  was 0.0891, and the changes in the drag coefficient and pitching moment coefficient were less than 0.2. Along point B to point C, the angle of attack increased from  $20.57^\circ$  to  $21.62^\circ$ , the lift coefficient increased nonlinearly, but the slope decreased slightly, and the drag coefficient and pitching moment coefficient increased rapidly. Along point C to point D, the angle of attack changed from  $21.67^\circ$  to  $22^\circ$ , the lift coefficient continued to increase nonlinearly, the angle change was only  $0.33^\circ$ , and the drag coefficient and pitching moment coefficient suddenly increased to the maximum value. (2) The downstroke process: Along point D to point E, the angle of attack changed from  $22^\circ$  to  $20.41^\circ$ , the angle change was only  $1.6^\circ$ , the lift coefficient dropped sharply by approximately 75%, and the drag coefficient and pitching moment coefficient decreased by 80%. Along point E to point F, the lift coefficient was restored, the drag coefficient and pitching moment coefficient fluctuated, and the aerodynamic force appeared to have a secondary peak. Along point F to point A,

the lift force, drag coefficient, and pitching moment coefficient gradually returned to the initial state.

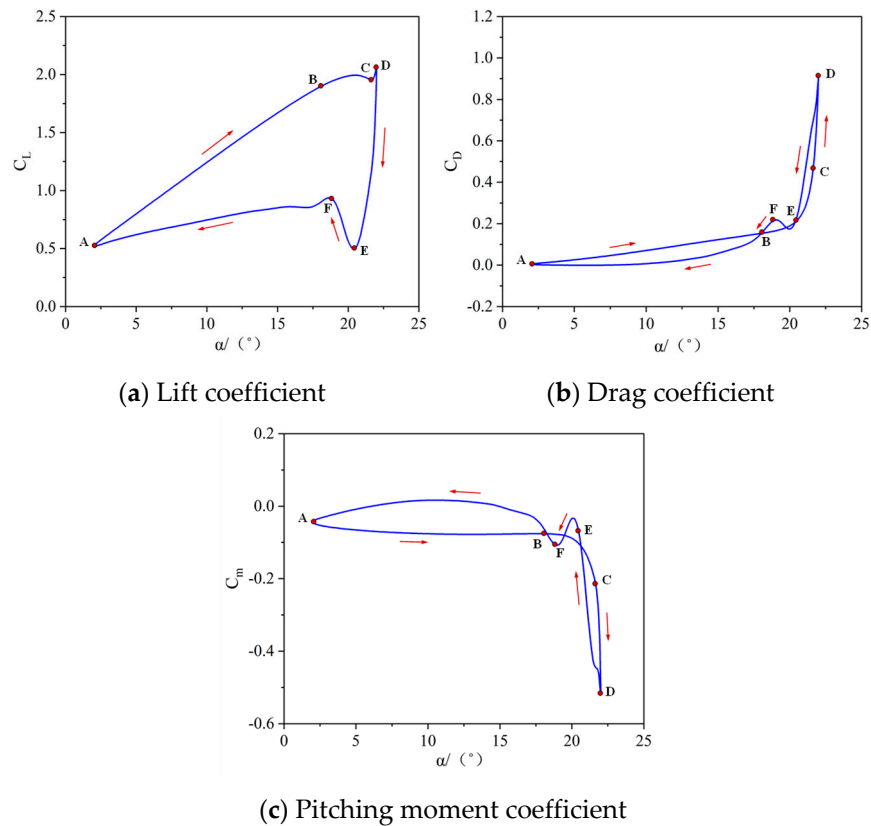


**Figure 4.** Aerodynamic force coefficients of NACA63-218 airfoil.

The complex variations in the aerodynamic characteristics during the dynamic stall of airfoils reflects the intricate evolution of different vortex structures. To further study the main controlling mechanisms of the nonlinear hysteresis of aerodynamic forces caused by different vortex structures in the dynamic stall process, it was necessary to analyze the flow characteristics related to the generation, convection, separation, and evolution of different vortex structures during dynamic stall.

### 3.2. Evolution Process of Different Vortex Structures during Dynamic Stall

Based on the analysis of the spatiotemporal evolution of the flow field structure and surface pressure distribution, the evolution process of different vortex structures (leading-edge vortex, trailing-edge vortex, shear vortex, dynamic stall vortex, secondary vortex) in dynamic stall could be identified, in addition to the active control vortex mechanism that affected the aerodynamic nonlinear hysteresis. Figure 5 shows the  $C_p$  contour,  $Q$  contour, and surface pressure distribution within a cycle of the airfoil's dynamic stall process.

From the figure, it was observed that based on the flow structures depicted by the pressure contour  $C_p$  and the variation in surface pressure distribution, the flow characteristics within a cycle can be divided into the following stages:

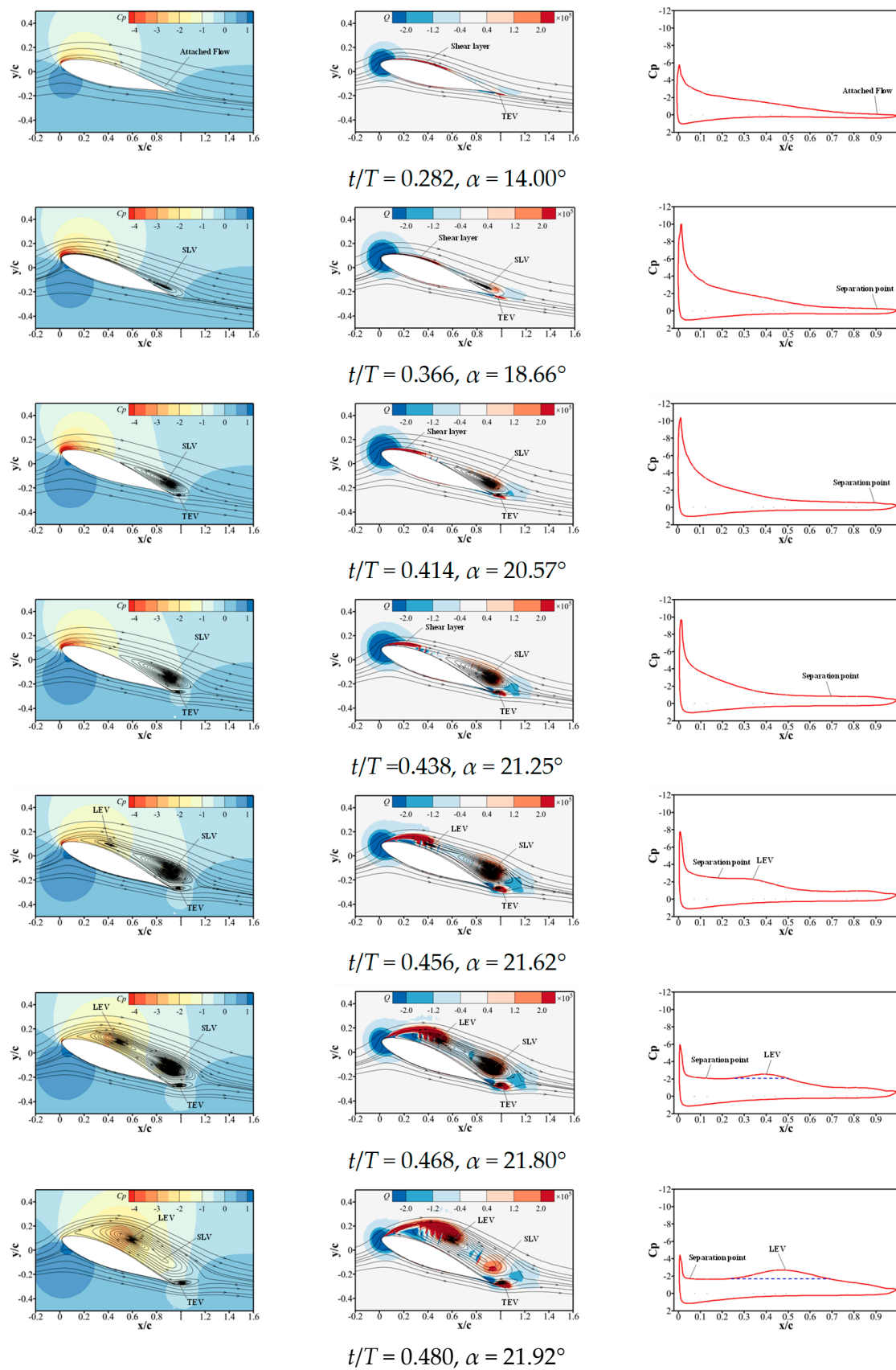


Figure 5. Cont.

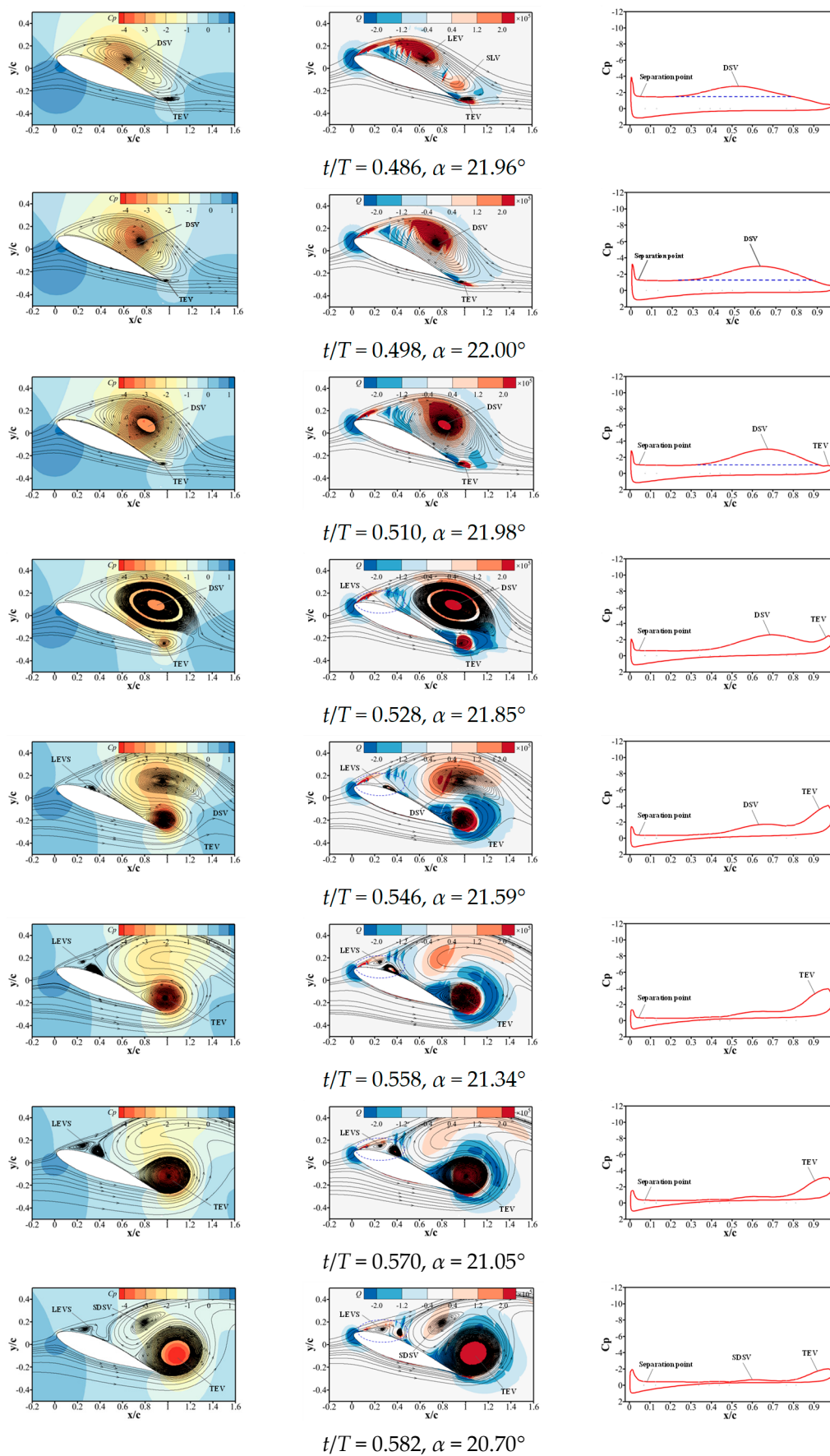
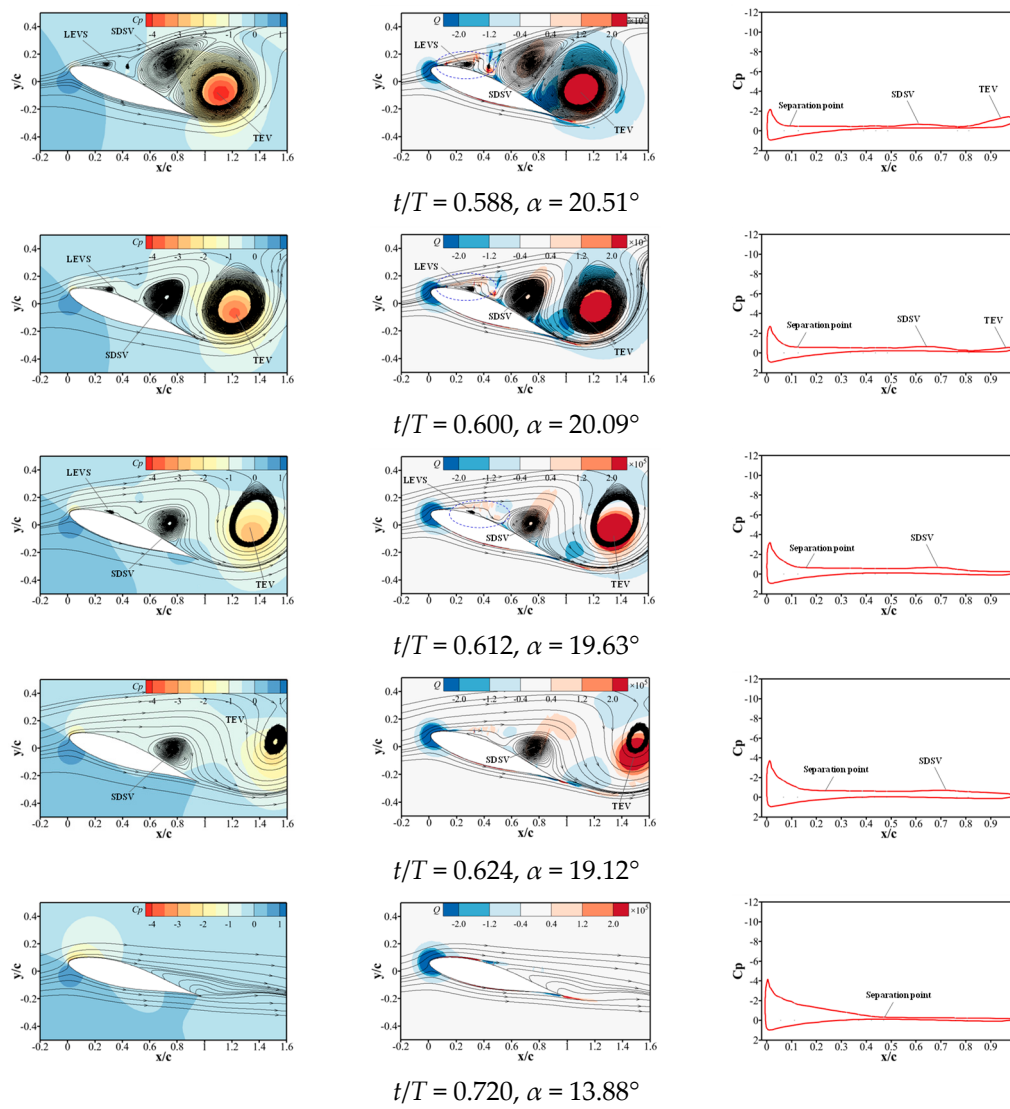


Figure 5. Cont.



**Figure 5.** Evolution process of  $C_p$  flow structure and pressure distribution within a cycle.

Upstroke process: (1) As the angle of attack increased to  $14^\circ$ , it was shown that the flow remained attached without any separation of the flow structure depicted from the  $C_p$  contour, the  $Q$  contour, or the surface pressure distribution. The lift coefficient increased linearly with the angle of attack, while the changes in the drag coefficient and pitching moment coefficient were relatively small. (2) As the angle of attack continued to increase, when  $\alpha = 18.66^\circ$ , the  $C_p$  contour and the  $Q$  contour showed a small range of flow separation at the trailing edge, forming an SLV (shear layer vortex). The pressure distribution was characterized by a “pressure plateau” with local small-scale vortex separation at the trailing edge, but the peak value of the pressure coefficient at the upper airfoil edge continued to increase. (3) As the angle of attack continued to increase, such as from  $20.57^\circ$  to  $21.25^\circ$ , the strength of the SLV gradually increased (seen from the  $Q$  contour), and a large-scale flow separation occurred at the trailing edge. The pressure distribution was characterized by a “pressure plateau”, indicating large-scale vortex separation at the trailing edge. At the sharp trailing edge of the lower airfoil, a trailing-edge vortex (TEV) was formed due to the shearing effect of the airflow, but its strength was weak. The flow structure showed that there were two clear structures at the trailing edge. The pressure distribution was characterized by the vortex separation point moving upstream from  $0.90c$  to  $0.61c$  at a velocity of  $0.069V_\infty$ . The peak value of the pressure coefficient on the upper surface of the leading edge continued to increase. As a result, the lift coefficient exhibited nonlinear

growth, although the slope slightly decreased. Due to the dominant influence of the SLV, the drag coefficient and pitching moment coefficient increase. (4) As the angle of attack continued to increase, when  $\alpha = 21.62^\circ$ , under the influence of an adverse pressure gradient, vorticity accumulated at the position  $x/c = 0.35$  on the leading edge, forming a leading-edge vortex (LEV). As the angle of attack increased from  $\alpha = 21.62^\circ$  to  $\alpha = 21.92^\circ$ , the LEV rapidly merged with the SLV (seen from the  $C_p$  contour and the Q contour). The strength of the LEV increased and there was a sudden burst of vorticity. The trailing-edge vortex (TEV) remained relatively unchanged. The flow structure showed the presence of three vortex structures. The pressure distribution indicated that, at the position  $x/c = 0.35$ , there was a convex increase in the pressure coefficient. The "pressure plateau" underwent a sudden jump, transitioning from  $C_p \approx 1$  to  $C_p \approx 2$ . The separation point moved from  $0.68 c$  to  $0.18 c$  and the peak pressure coefficient on the leading edge was reduced by 50%. The nonlinear increase in the lift coefficient was attributed to the vortex lift generated by the LEV. (5) As the angle of attack increased from  $\alpha = 21.92^\circ$  to  $\alpha = 22^\circ$ , the vortex at the leading edge started to roll up, forming a larger-scale vortex structure that covered the entire upper surface and moved toward the trailing edge, which became the dynamic stall vortex (DSV). The trailing-edge vortex (TEV) remained relatively unchanged and the flow structure exhibited the presence of two vortex structures. The pressure distribution was characterized by a continuous increase in the area of the bulging region in the pressure coefficient. At the same time, the peak value of the pressure coefficient on the leading edge of the upper airfoil edge exhibited a continuous decrease. The DSV moved downstream at a speed of  $0.13V_\infty$ , which was approximately one-third of the free-stream velocity. This downstream migration of the DSV caused the pressure center to shift toward the rear. The DSV's dominant control and induction effect contribute to a nonlinear increase in the lift coefficient. Additionally, the drag coefficient and pitching moment coefficient increased to their maximum values, resulting in a significant nose-down moment.

Downstroke process: (1) From the maximum angle of attack of  $21.98^\circ$  to  $21.59^\circ$ , the DSV left the airfoil. The pressure distribution was characterized by a gradual decrease in the pressure coefficient at the  $x/c = 0.68$  position. At the trailing edge of the airfoil, the flow structure showed that the strength of the TEV was enhanced, and the airflow was adsorbed from the lower surface to the upper surface. The pressure distribution was characterized by an increase in the pressure coefficient at the trailing edge, and the pressure coefficient of the lower airfoil ( $x/c = 0.9\sim 1.0$ ) The pressure coefficient decreased and the peak value of the pressure coefficient and the position of the separation point on the upper airfoil remained basically unchanged. Therefore, the lift coefficient, drag coefficient, and pitching moment coefficient gradually decreased. (2) From  $21.34^\circ$  pitching down to  $21.05^\circ$ , the flow structure showed that the DSV dissipated rapidly, the vortex structure basically disappeared completely, and the intensity of the TEV increased. In addition, the vortex scale increased to two to three times that of the upstroke process and formed a negative impact on the upper wing surface, a strong induction effect, and a reduced pressure coefficient. Simultaneously, a leading-edge vortex system (LEVS) formed at the leading edge of the upper surface, and the vortex structure gradually became more complex. The lift coefficient, drag coefficient, and pitching moment coefficient all decreased sharply, reaching 75% of their maximum values. (3) Descending from  $20.70^\circ$  to  $20.09^\circ$ , the flow structure showed the gradual disappearance of the LEVS, and the scale of the TEV continued to increase. It strongly induced low-energy fluid in the dissipation region of the dynamic stall vortex, forming a secondary dynamic stall vortex (SDSV). During this stage, the intensity of the SDSV continued to increase and gradually approached the airfoil surface. The pressure distribution was characterized by a secondary convexity in the pressure coefficient at  $x/c = 0.65$ , but with a lower peak. At the trailing edge, although the scale of the TEV increased, the peak of the pressure coefficient decreased. (4) From  $19.63^\circ$  to  $19.12^\circ$ , the flow structure showed that the SDSV migrated downstream along the airfoil, exhibiting secondary stall, and the aerodynamic force and pitch moment coefficients showed fluctuations with a secondary peak in aerodynamic force. The TEV gradually separated from

the trailing-edge position and the dissipation disappeared. The pressure distribution was characterized by an increase in the pressure coefficient peak at the leading edge of the upper surface and the separation point gradually moved from  $0.10c$  along the leading edge to  $0.28c$  at a speed of  $0.123 V_\infty$ . (5) Decreasing from  $13.88^\circ$  to the minimum angle of attack, at this stage, the pressure distribution was characterized by the separation point rapidly moving to  $0.68c$  at a speed of  $0.069 V_\infty$ . In addition, the pressure coefficient at the leading edge of the upper surface gradually recovered. Therefore, the lift coefficient began to recover but was lower than the corresponding upstroke value at the same angle of attack. This was mainly due to the separation on the upper surface of the airfoil (complete attachment during the upstroke). The drag coefficient was lower than the corresponding upstroke value, while the pitching moment coefficient was larger than the corresponding upstroke value. The delayed movement of the separation point resulted in an asymmetric pressure distribution, which was a major factor influencing the nonlinear hysteresis of the aerodynamics.

In conclusion, the complex nonlinear hysteresis characteristics of aerodynamics in dynamic stall arose from the evolution process of different vortex structures and motion characteristics during dynamic stall. During the pitching-up phase, under the influence of an adverse pressure gradient, a separated leading vortex (SLV) formed at the trailing edge. With the continuous increase in the angle of attack, due to the sustained supply of vorticity from the bottom layer to the boundary layer, vorticity accumulated at the airfoil's leading edge, forming a leading-edge vortex (LEV). As the angle of attack continued to increase, the LEV and SLV quickly merged, and the vorticity underwent a rapid burst, resulting in convection toward the trailing edge to form a DSV. The aerodynamic coefficients and pitching moment coefficient increased to their maximum values. During the pitching-down phase, the DSV gradually dissipated, and the strength and scale of the TEV increased. This induced the low-energy fluid in the dynamic stall vortex dissipation region to form an SDSV. This led to a secondary stall and the aerodynamic coefficients exhibited a secondary peak. The DSV and SLV were the main control vortex mechanisms influencing the increase in the aerodynamic coefficients, pitching moment coefficient, and nonlinear hysteresis.

Note: The TEV was a vortex structure near the trailing edge. The airflow was adsorbed from the lower surface to the upper surface and the shear layer rolled up to form a vortex. The vortex was fixed near the trailing edge, so it was called a trailing-edge vortex. The SLV was the vortex formed by the shear layer separation due to the flow detachment at a high Reynolds number, also known as a shear separation vortex. The LEV could be considered the initial stage of the DSV. As the LEV gradually strengthened, when it could not maintain its current scale, it detached from the leading edge of the airfoil and migrated downstream, forming the dynamic stall vortex. The SDSV was a secondary vortex structure, reformed due to the inductive effect of the TEV on the low-energy fluid in the dissipation region of the DSV.

Figure 6 shows the variation in the pitching moment coefficient within a cycle of the dynamic process. From the figure, it can be observed that during the pitch-up phase, the LEV quickly merged with the SLV, forming a DSV. This was an important source of the increase in aerodynamic force and pitching moment coefficient, leading to a peak in the aerodynamic force. During the pitch-down phase, the formation of an SDSV resulted in a secondary peak in both the aerodynamic force and pitching moment coefficients.

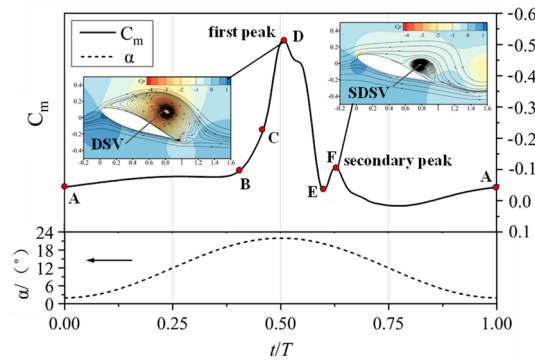


**Figure 6.** Characteristics of pitch torque coefficient variation within a cycle (The “A–F” here is consistent with the “A–F” in Figure 4).

#### 4. Air-Blow Control of Dynamic Stall

##### 4.1. Proposal of Air-Blow Control

Based on the analysis of the spatiotemporal evolution characteristics of the flow structure and surface pressure distribution of the pressure contour  $C_p$ , the SLV and the DSV were the main control vortices that increased the aerodynamic force and pitching moment coefficient during the dynamic stall process. Therefore, without changing the aerodynamic shape and structural form of the airfoil, if it was necessary to control the negative damping of dynamic stall, control measures needed to be designed based on the formation and convergence of the DSV and SLV. In response to control of the DSV and SLV, the concept of distributed air blow control was proposed, as shown in Figure 7. The leading edge of the airfoil was equipped with three distributed jet outlets, located at 5%  $c$ , 10%  $c$ , and 30%  $c$  from the leading edge, where  $c$  was the chord length. The gap at the outlet  $h$  was 1 mm and the ratio of  $h$  to  $c$  was 0.002857. The outlet angle was inclined at an angle  $\theta$  of  $30^\circ$  to the local airfoil surface. The blowing positions at 5%  $c$  and 10%  $c$  mainly controlled the generation of an LEV and suppressed the formation of the DSV. The blowing position at 30%  $c$  mainly controlled the strength of the SLV. To adapt to engineering applications, the jet outlets were set as pressure outlet boundary conditions, and by altering the pressure values at the jet outlets, control over the jet blowing velocity could be achieved.

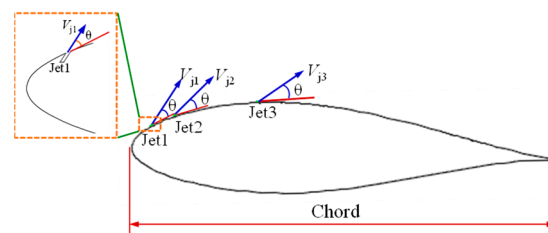


**Figure 7.** Leading-edge distributed blowing control.

The blowing momentum coefficient  $C_\mu$  was used to measure the strength of the blowing and it was defined as follows:

$$C_\mu = \frac{\dot{m}_j V_j}{\frac{1}{2} \rho_\infty V_\infty^2 c} \quad (5)$$

$$V_j = \sqrt{\frac{2\gamma R T_j}{\gamma - 1} \left[ 1 - \left( \frac{P_j}{P_0} \right)^{\frac{\gamma}{\gamma - 1}} \right]} \quad (6)$$

Here,  $\dot{m}_j$  was the mass flow rate of the  $j$ th jet, and  $\dot{m}_j = \rho_j V_j h$ , where  $h$  was the width of the jet exit,  $\rho_j$  was the density of the  $j$ th jet,  $V_j$  was the jet velocity at the exit (expansion to the jet velocity when isentropically expanded to the incoming static pressure),  $\rho_\infty$  was

the density of the incoming flow,  $V_\infty$  was the incoming flow velocity, and  $c$  was the chord length of the airfoil.  $P_0$  was the total pressure of the incoming flow,  $T_j$  and  $P_j$  were the total temperature and total pressure, respectively, at the jet exit,  $R$  was the gas constant, and  $\gamma$  was the specific heat ratio.

It is shown in Figure 8 that the aerodynamic coefficient comparison under the control of different combinations of blowing positions resulted in  $M = 0.3$ ,  $Re = 2.41 \times 10^6$ , and an angle of attack variation pattern  $\alpha = 12^\circ + 10^\circ \sin(2kt)$ , with  $k = 0.129$ , the total pressure at the jet outlet  $P_j = 110,545 \text{ Pa}$ , the total temperature  $T_j = 288.15 \text{ K}$ , and the blowing positions at  $x/c = 5\%$ ,  $10\%$ , and  $30\%$ , respectively.

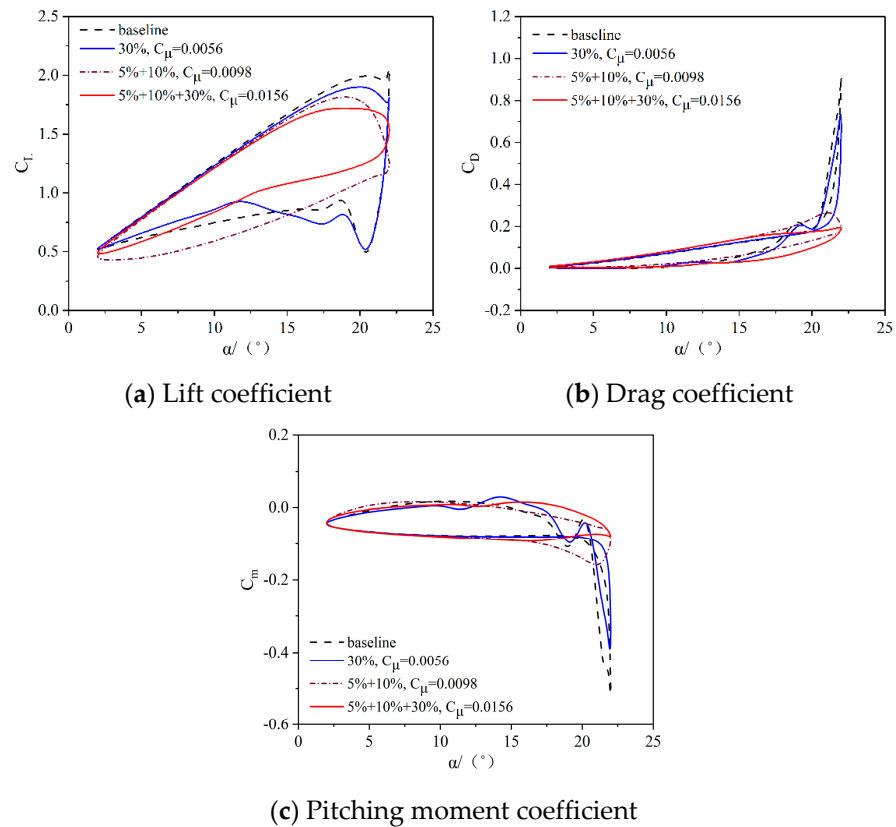


**Figure 8.** Aerodynamic coefficients of combined control with different blowing positions.

It was shown that the combination control of the blowing positions had a significant impact on the aerodynamics of dynamic stall. During the blowing control, both the drag and pitching moment coefficients of the airfoil decreased. Within the linear range of lift, the combined control over the air blowing at different positions had a minor impact on the lift coefficient at the same angle of attack, and the effect on the slope of the lift curve in the linear range was also minimal. Comparison of different combinations of air blowing positions: (1) When the air blowing position was at  $x/c = 30\%$ , compared to the baseline state, the change in the lift coefficient at the stall angle of attack was the most significant. At the maximum angle of attack, the lift coefficient still showed a nonlinear increase. The reduction in the peak values of drag and pitching moment coefficients was 20%. (2) When the air blowing positions were at  $x/c = 5\%$  and  $10\%$ , the reduction in the peak values of the drag and pitching moment coefficients could reach 70%. However, around an angle of attack of  $19^\circ$ , the lift coefficient experienced a sharp decrease. In the downward pitching phase, compared to the baseline state, there was an increase in the hysteresis area of the lift coefficient curve. (3) When the air blowing positions were at  $x/c = 5\%$ ,  $10\%$ , and  $30\%$ , compared to the baseline state, the hysteresis curve of the lift coefficient changed smoothly with the variation in the angle of attack, and the hysteresis loop area decreased by 41%. Around an angle of attack of  $19^\circ$ , there was no fluctuation in the drag and pitching moment coefficients, and

the reduction in the peak values of the drag and pitching moment coefficients could reach 80%. The secondary peaks in the aerodynamic coefficients disappeared and the hysteresis loop area of the lift coefficient decreased by 41%.

Figure 9 shows the comparison results of the  $C_p$  contour, the  $Q$  contour, and the surface pressure distribution controlled by different blowing position combinations when the maximum angle of attack  $\alpha = 22^\circ$ : (1) When the blowing position was at  $x/c = 30\%$ , from the pressure distribution, it could be seen that the blowing position was downstream of the separation point, and the inhibitory effect on the aerodynamics was relatively weak. However, due to the influence of the jet vortex, the strength of the DSV decreased, the area of the pressure distribution bulge decreased, and the peak values of the drag and pitch moment coefficients decreased. As was seen from the pressure distribution  $C_p$ , the strength and scale of the DSV decreased, but it still remained the main controlling vortex affecting the increase in the aerodynamic forces and pitch moment coefficients. Due to the inductive effect of the DSV, vortex lift was generated, and the lift coefficient curve still exhibited a small-range nonlinear increase. (2) When the blowing positions were at  $x/c = 5\%$  and  $10\%$ , it could be observed from the pressure distribution  $C_p$  that the DSV was suppressed, and the flow structure exhibited two vortex structures, the SLV and TEV. Due to the strong induction effect of the SLV on the TEV, the intensity of the TEV was enhanced. From the pressure distribution, it could be observed that the region of pressure rise disappeared. The pressure distribution indicated a “pressure plateau” caused by the large-scale vortex separation on the upper surface and the separation point was located at  $x/c = 0.33$ . This indicated that the SLV was the main controlling vortex affecting the increase in the aerodynamic force and pitching moment coefficients at this time. Due to the dominant controlling effect of the SLV, the lift coefficient began to experience stall around  $19^\circ$ , dropping sharply. The reduction in the drag and pitching moment coefficients reached 70%. (3) When the blowing positions were at  $x/c = 5\%$ ,  $10\%$ , and  $30\%$ , from the pressure distribution  $C_p$ , it could be observed that there were two vortex structures in the flow, the SLV and TEV. Compared with  $x/c = 5\%$  and  $10\%$ , the blowing jet at  $x/c = 30\%$  suppressed the intensity of the EV due to the inhibition of the SLV. Therefore, the large-scale flow separation was inhibited. From the pressure distribution, it could be observed that the separation point had moved to  $x/c = 0.56$ . This indicated that the distributed blowing control ( $x/c = 5\%$ ,  $10\%$ , and  $30\%$ ) not only controlled the formation of the DSV but also had a controlling effect on the SLV, demonstrating a dual control effect.

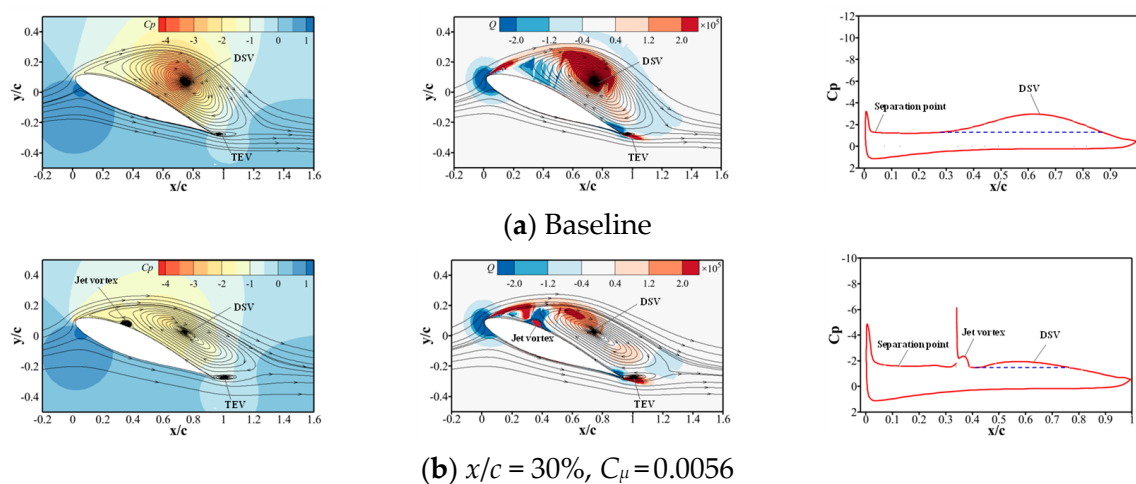
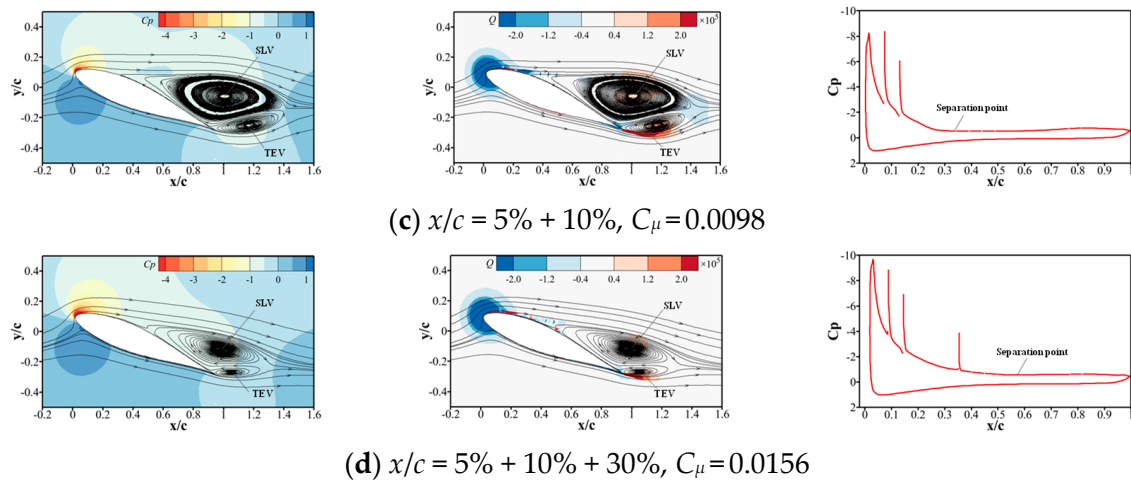


Figure 9. Cont.



**Figure 9.**  $C_p$  contour,  $Q$  contour, and pressure distribution of the airfoil under combined control state at different blowing positions.

#### 4.2. Effect of the Blowing Coefficient

The comparison of aerodynamic coefficients of different blowing coefficients can be seen in Figure 10, with  $M = 0.3$ ,  $Re = 2.41 \times 10^6$ , the change pattern of the angle of attack  $\alpha = 12^\circ + 10^\circ \sin(2kt)$ ,  $k = 0.129$ , the temperature at the jet outlet  $T_j = 288.15$  K, and the blowing positions at  $x/c = 5\%$ ,  $10\%$ , and  $30\%$ . When the total pressure at the jet nozzle exit  $P_j$  changed, the variation in the stagnation ring area  $C_{L,S}$ , the peak lift coefficient  $C_{L,peak}$ , the peak drag coefficient  $C_{D,max}$ , and the peak pitch moment coefficient  $C_{m,min}$  were compared with different blowing coefficients  $C_\mu$  for control.

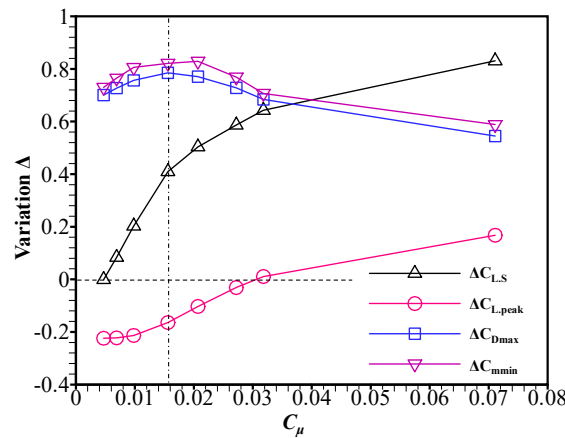


**Figure 10.** Comparison of aerodynamic coefficients of different blowing coefficients.

From the graph, it was observed that with an increase in the blowing coefficient  $C_\mu$ , corresponding to an increase in the jet exit pressure  $P_j$ , the peak variation in the drag coefficient  $\Delta C_{D,max}$  and the peak variation in the pitch moment coefficient  $\Delta C_{m,min}$  initially showed a gradual increase around  $C_\mu = 0.016$ , reaching the maximum value. The variation in  $\Delta C_{D,max}$  and  $\Delta C_{m,min}$  reached 80%. With the continued increase in the blowing coefficient ( $C_\mu$ ), the variations in the peak drag and pitch moment coefficients gradually decreased. Around  $C_\mu = 0.07$ , the variations in  $\Delta C_{D,max}$  and  $\Delta C_{m,min}$  dropped to less than 60%. This indicated the existence of an optimal blowing coefficient. Beyond this upper limit, the effect of the blowing control no longer showed a significant improvement. With the increase in the blowing coefficient ( $C_\mu$ ), significant changes were observed in the variation in the stagnation ring area ( $\Delta C_{L,S}$ ) and the peak lift coefficient ( $\Delta C_{L,peak}$ ) when  $C_\mu$  was less than 0.03. However, when  $C_\mu$  exceeded 0.03, the changes in the stagnation ring area ( $\Delta C_{L,S}$ ) and the peak lift coefficient ( $\Delta C_{L,peak}$ ) became less pronounced.

In order to compare the aerodynamic coefficient variations under different jet exit pressures, the results of the aerodynamic coefficient variations for blowing coefficients ( $C_{\mu}$ ) of 0.0069, 0.0156, 0.0272, and 0.0711 can be seen in Figure 11. From the graph, it can be observed that when the blowing coefficient ( $C_{\mu}$ ) was 0.0069, despite a significant reduction in the drag and pitch moment coefficients, there was a decrease in the peak lift coefficient during the upstroke and the lift coefficient during the downstroke. Additionally, the area of the stagnation ring increased. When the blowing coefficient ( $C_{\mu}$ ) was 0.016, there was a significant decrease in the peak values of the drag and pitch moment coefficients, an increase in the lift coefficient, and a smooth variation in the aerodynamic coefficients with an angle of attack. The area of the stagnation ring also decreased. When the blowing coefficient was 0.0711, there was a 16% increase in the peak lift coefficient, but the lift curve also underwent a significant shift. Compared to  $C_{\mu} = 0.016$ , at the maximum angle of attack, the angle of attack changed by only  $1^{\circ}$ . Furthermore, the lift coefficient showed a sharp decrease, followed by a rapid recovery, indicating a prominent peak discontinuity. The peak values of the drag and pitch moment coefficients increased, exhibiting the characteristics of sharp peaks in both the upward and downward directions, with rapid variations. Rapid changes in aerodynamic forces could have a significant impact on the control system and are an important source of control loads for helicopter swashplate manipulation. The comparison of the aerodynamic coefficient variations under different jet exit pressures illustrates the existence of an optimal blowing coefficient. Beyond this upper limit, not only did the effectiveness of the blowing control fail to show a significant improvement but it also led to excessive control loads.

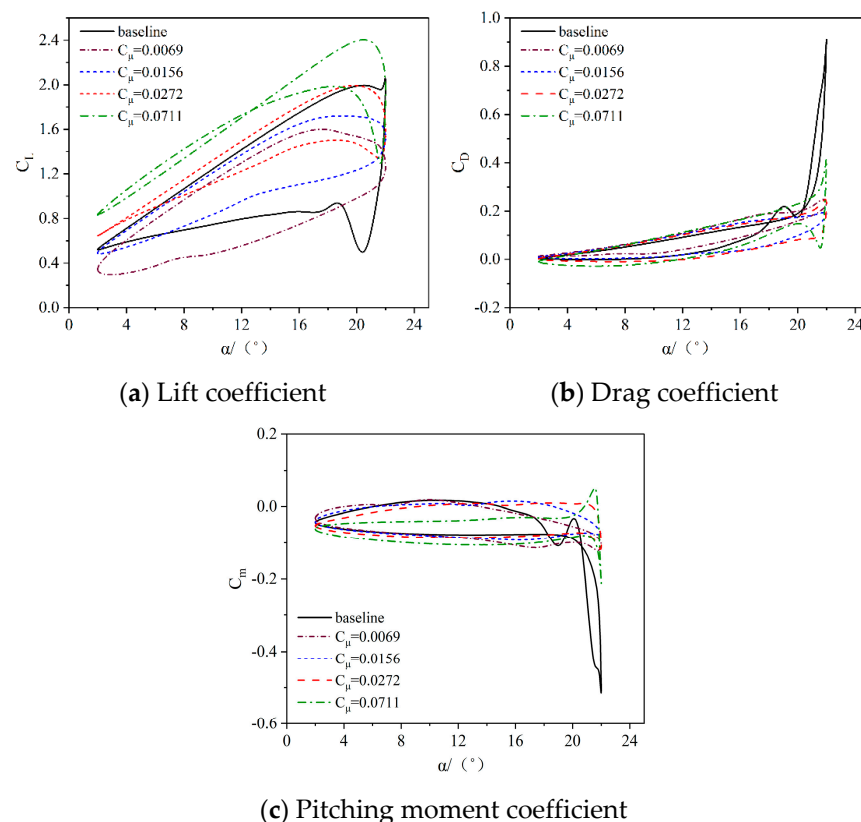


**Figure 11.** Comparison of aerodynamic coefficients under different blowing coefficients.

## 5. Effect of Motion Parameters

To implement distributed blowing control in engineering applications, it was crucial to delve into its operational scope. This study focused on the dynamic stall control effectiveness of distributed blowing control under multiple operating conditions, particularly examining the motion parameters during dynamic stall. The blowing locations were situ-

ated at  $x/c = 5\%$ ,  $10\%$ , and  $30\%$ , with a specified jet exit total pressure  $P_j = 110545\text{Pa}$  and total temperature  $T_j = 288.15\text{K}$ .

The reference conditions were as follows:  $M = 0.3$ ,  $Re = 2.41 \times 10^6$ , and the variation pattern of the angle of attack ( $\alpha$ ) followed  $\alpha = 12^\circ + 10^\circ \sin(2kt)$ , with  $k = 0.129$ . The sensitivity parameter analysis involved changing only the parameter under consideration, while keeping the other parameters consistent with the reference conditions.

### 5.1. Mean Angle of Attack

Simulations were performed for three scenarios with the average angles of attack ( $\alpha_0$ ) set at  $10^\circ$ ,  $12^\circ$ , and  $14^\circ$ . Figure 12 illustrates the impact of the distributed air blowing control on the dynamic stall characteristics of the airfoil under different average angles of attack, while maintaining a constant total pressure at the jet outlet. From the graph, it could be observed that the variation in the average angle of attack had a minimal impact on the blowing coefficient. With the other conditions held constant, at an average angle of attack of  $10^\circ$ , the lift coefficient increased with the angle of attack. Near the maximum angle of attack, the lift coefficient curve exhibited a sharp decrease, indicating that the dynamic stall was primarily controlled by the SLV. Therefore, the impact on the pressure distribution was limited, resulting in lower peak values for the drag and pitch moment coefficients. The stall curve exhibited a clockwise “∞”-shaped pattern. At an average angle of attack of  $12^\circ$ , the dynamic stall characteristics of the airfoil intensified. With the variation in the angle of attack, the lift coefficient gradually increased. Near the maximum angle of attack, the lift coefficient decreased due to the onset of separation on the upper surface of the wing. With a further increase in the angle of attack, the lift coefficient exhibited nonlinear growth. The drag and pitch moment coefficients sharply increased and the area under the stall curve expanded. The DSV was the primary controlling vortex, leading to an increase in the aerodynamic coefficient peaks. In the pitching-down phase, unlike at lower average angles of attack, the influence of the TEV contributed to a secondary dynamic stall process, resulting in significant fluctuations in the aerodynamic coefficients. With the continued increase in the average angle of attack, the dynamic stall characteristics intensified. This indicated that the strength of the DSV also increased with higher average angles of attack. After implementing distributed blowing control, at an average angle of attack of  $10^\circ$ , the dynamic stall vortex primarily controlled by the SLV was suppressed. The vortex-induced lift associated with the dynamic stall vortex diminished, resulting in a reduction in the peak lift coefficient, a decrease in the stagnation ring area, and a 50% reduction in the peak values of the drag and pitch moment coefficients. The area of the lift stagnation ring decreased by 47%. At an average angle of attack of  $12^\circ$ , it could be observed from the lift coefficient curve that the nonlinear increase near the maximum angle of attack disappeared. This indicated that distributed blowing control had mitigated the formation of the DSV. At this time, the SLV became the primary controlling vortex influencing the peak aerodynamic coefficients. The peak values of the drag and pitch moment coefficients decreased by 80% and the area of the lift stagnation ring decreased by 41%.

The  $C_p$  contour and Q contour of the airfoil at different mean angles of attack can be seen in Figure 13. It can be observed that (1) at an average angle of attack of 10 degrees, the SLV was the primary controlling vortex structure influencing the dynamic stall, playing a major role in the aerodynamic forces during dynamic stall, albeit with a lower peak. With the implementation of blow control, the intensity of the SLV weakened, resulting in a reduction in the peak drag and pitch moment coefficients. (2) At average angles of attack of  $12^\circ$  and  $14^\circ$ , the formation of the DSV became the primary controlling vortex structure influencing the increase in aerodynamic forces, leading to a sharp increase in the peak drag and pitch moment coefficients. After the implementation of blow control, the formation of the LEV was suppressed, leading to the disappearance of the DSV. The secondary SLV became the primary controlling vortex influencing the aerodynamic forces. Due to the relatively minor impact of the SLV on the surface pressure distribution, the peak aerodynamic coefficient was lower.

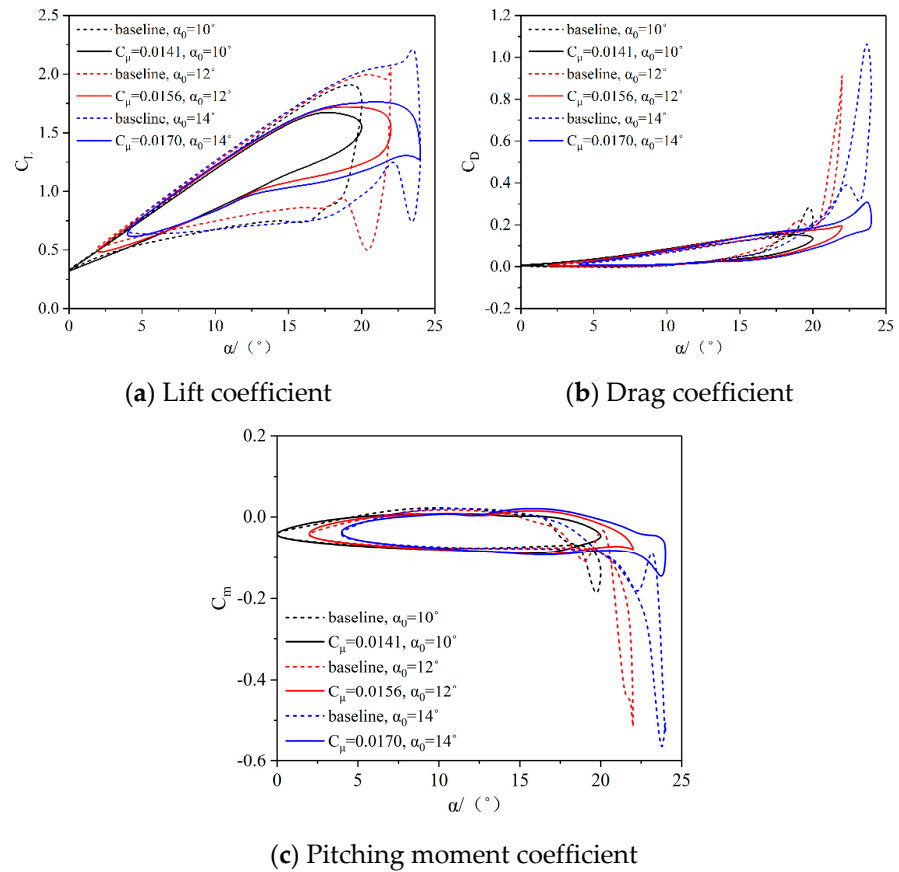


Figure 12. Aerodynamic coefficients at different mean angles of attack.

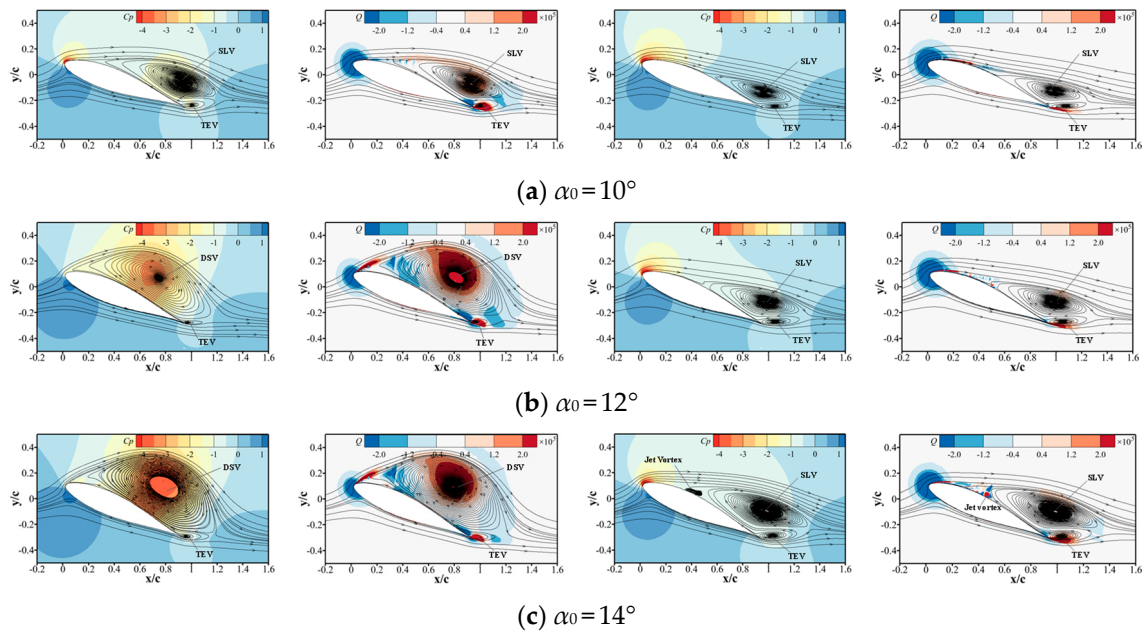
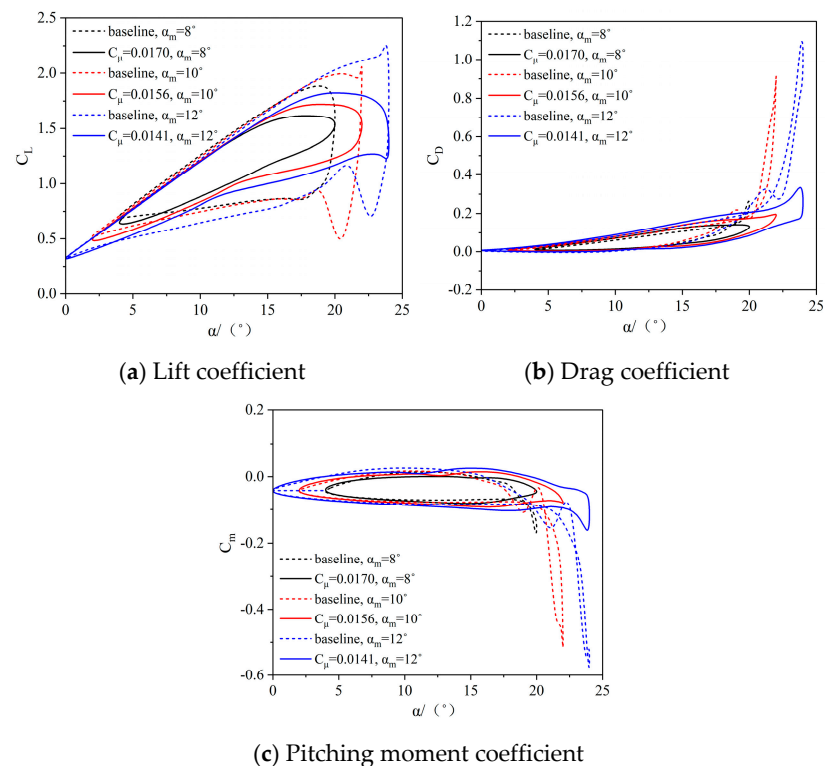


Figure 13.  $C_p$  contour and  $Q$  contour of the airfoil at different mean angles of attack (baseline is in left column and controlled in right).

### 5.2. Amplitude of the Angle of Attack

A comparison of the aerodynamic forces during dynamic stall for different amplitudes of the angle of attack ( $\alpha_m$ ) of  $8^\circ$ ,  $10^\circ$ , and  $12^\circ$  can be seen in Figure 14, with a constant jet exit

total pressure. The comparison was based on distributed blowing control under different amplitudes of the angle of attack. From the curves in Figure 14, it can be observed that, with an increase in the amplitude of the angle of attack, the dynamic stall characteristics of the airfoil continually intensified. The peak values of the drag and pitch moment coefficients increased and the stall effect became more pronounced. The area under the stall curve increased with the growth of the angle of attack amplitude. At a low-amplitude angle of attack ( $\alpha_m = 8^\circ$ ), the nonlinear increase in the lift coefficient did not occur, and the peak aerodynamic coefficients during dynamic stall were primarily controlled by the SLV. At large amplitudes of the angle of attack ( $\alpha_m = 10^\circ$  and  $12^\circ$ ), near the maximum angle of attack, the lift coefficient exhibited a nonlinear increase with an increase in the angle of attack. The peak values of the drag and pitch moment coefficients sharply increased and the peak aerodynamic coefficients were primarily controlled by the DSV. Distributed blowing control could suppress the occurrence of the DSV and the nonlinear peak in the aerodynamic forces, thereby mitigating load fluctuations. At different amplitudes of the angle of attack, distributed blowing control could suppress the peak values of the drag and pitch moment coefficients. Under a small-amplitude angle of attack ( $\alpha_m = 8^\circ$ ), the peak drag coefficient decreased by 46%, the peak pitch moment coefficient decreased by 74%, and the hysteresis loop area of the lift coefficient was reduced by 50%. At a large-amplitude angle of attack ( $\alpha_m = 12^\circ$ ), the peak drag coefficient decreased by 70%, the peak pitch moment coefficient decreased by 72%, and the hysteresis loop area of the lift coefficient was reduced by 46%.



**Figure 14.** Aerodynamic coefficients at different amplitudes of angle of attack.

Figure 15 presents the  $C_p$  contour and the  $Q$  contour of the airfoil at different amplitudes of angle of attack. The following insights could be drawn from Figure 15: When the amplitude of angle of attack was  $8^\circ$ , the SLV served as the primary controlling vortex structure affecting the dynamic stall; it played a key role in the aerodynamic forces during dynamic stall. With the implementation of combined blow control, the weakening of the SLV intensity led to a reduction in the peak values of the drag and pitch moment coefficients. When the angle of attack amplitude was  $10^\circ$  and  $12^\circ$ , the DSV gradually formed, serving as the primary controlling vortex structure influencing the increase in the aerodynamic forces.

This led to a sharp increase in the peak values of the drag and pitch moment coefficients. With the application of blow control, the formation of the LEV was suppressed, causing the disappearance of the DSV structure. The SLV became the primary controlling vortex structure affecting the aerodynamic forces. As the impact of the SLV on the surface pressure distribution was relatively small, the peak aerodynamic coefficients were lower.

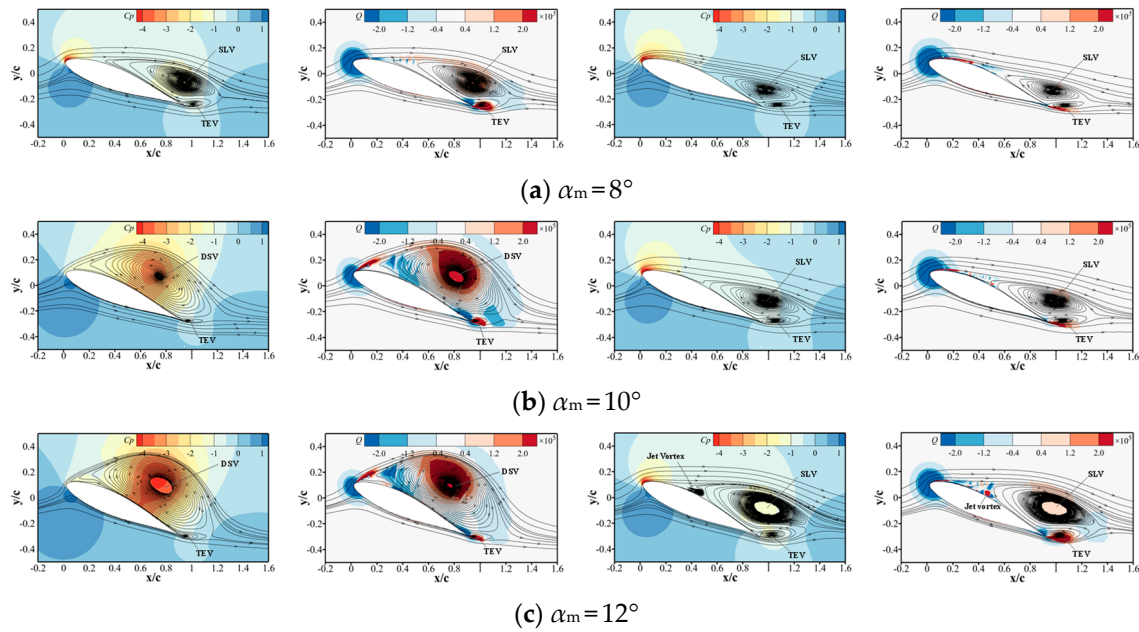


**Figure 15.**  $C_p$  contour and  $Q$  contour of the airfoil at different amplitudes of angle of attack (baseline is in left column and controlled in right).

### 5.3. Reduced Frequency

Reduced frequency is a dimensionless quantity commonly used in unstable aerodynamic conditions, and it is one of the parameters that defines the instability level of the problem [62]. Simulation of the dynamic stall was conducted for three different reduced frequencies ( $k = 0.097, 0.129, 0.162$ ). Figure 16 provides the coefficients at different reduced frequencies, the drag coefficient, and the pitch moment coefficient for the dynamic stall of the airfoil under a constant jet exit total pressure with distributed blowing control. From the graph, it can be observed that with a greater reduced frequency, the severity of the dynamic stall increased. The hysteresis loop area significantly enlarged, and the peak aerodynamic load, along with the corresponding angles of attack, also increased. Near the maximum angle of attack, the lift coefficient curve exhibited distinct variations. When the reduced frequency was  $k = 0.097$ , there was no nonlinear increase in the lift coefficient. Compared to high-frequency oscillations, the peak values of the drag and pitch moment coefficients were lower, and the increase in the peak aerodynamic coefficients was primarily controlled by the SLV. With a greater reduced frequency, around the maximum angle of attack, at a reduced frequency  $k = 0.129$ , the lift coefficient exhibited nonlinear growth. The peak values of the drag and pitch moment coefficients sharply increased and the DSV was the primary cause of the peak aerodynamic coefficients. When the reduced frequency was  $k = 0.162$ , the increase in oscillation frequency delayed the merging of the LEV and SLV. The lift coefficient exhibited a sudden nonlinear increase near the maximum angle of attack. Subsequently, during the downstroke process, the lift coefficient decreased, and the hysteresis loop in the lift coefficient curve exhibited closure near the maximum angle of attack. With an increase in reduced frequency, at the same angle of attack, the stall phenomenon became more pronounced in the airflow. During the downstroke process, the strength and scale of the TEV increased, and the position of the SDSV shifted forward. The amplitude of nonlinear fluctuations in the aerodynamic coefficients significantly increased and the

angle of attack for nonlinear fluctuations advanced. This led to a slower reattachment of the airflow during the downstroke process, resulting in an increased hysteresis area in the aerodynamic characteristic curve. At different reduced frequencies, distributed blowing control effectively suppressed the peak values of the drag and pitch moment coefficients, resulting in a reduction of 78% in the peak values of the drag and pitch moment coefficients. Additionally, the hysteresis loop area of the lift coefficient was decreased by 40%.

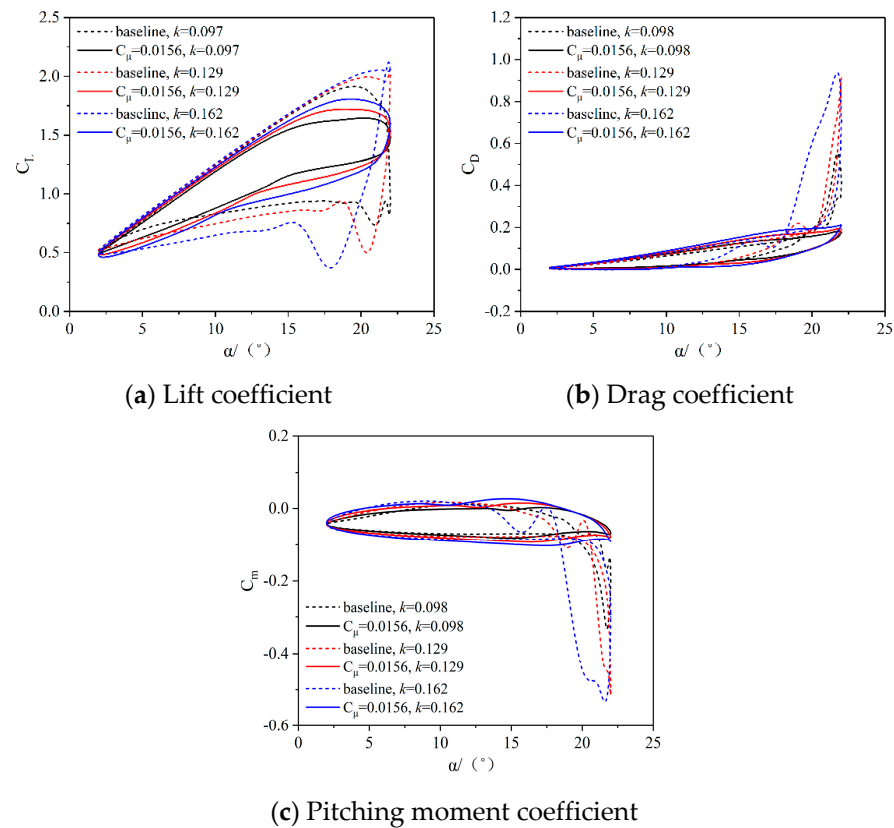


**Figure 16.** Aerodynamic coefficients at different reduced frequencies.

The  $C_p$  contour and  $Q$  contour under the peak pitch moment coefficient state with combined blow control are shown in Figure 17, with variations in reduced frequency. The following insights can be drawn from Figure 17: When the reduced frequency was  $k = 0.097$ , the DSV served as the primary controlling vortex structure influencing the aerodynamic forces during dynamic stall. The peak values of the drag and pitch moment coefficients significantly increased. Distributed blowing control could suppress the occurrence of the DSV and the nonlinear peak in aerodynamic forces. With an increase in reduced frequency, the intensity of the DSV gradually strengthened, leading to a sharp increase in the peak values of the drag and pitch moment coefficients. With the application of blow control, the formation of the LEV was suppressed, leading to the disappearance of the DSV. The SLV became the primary controlling vortex structure influencing the increase in the aerodynamic forces. Due to the relatively minor impact of the SLV on the surface pressure distribution, the peak aerodynamic coefficients were lower.

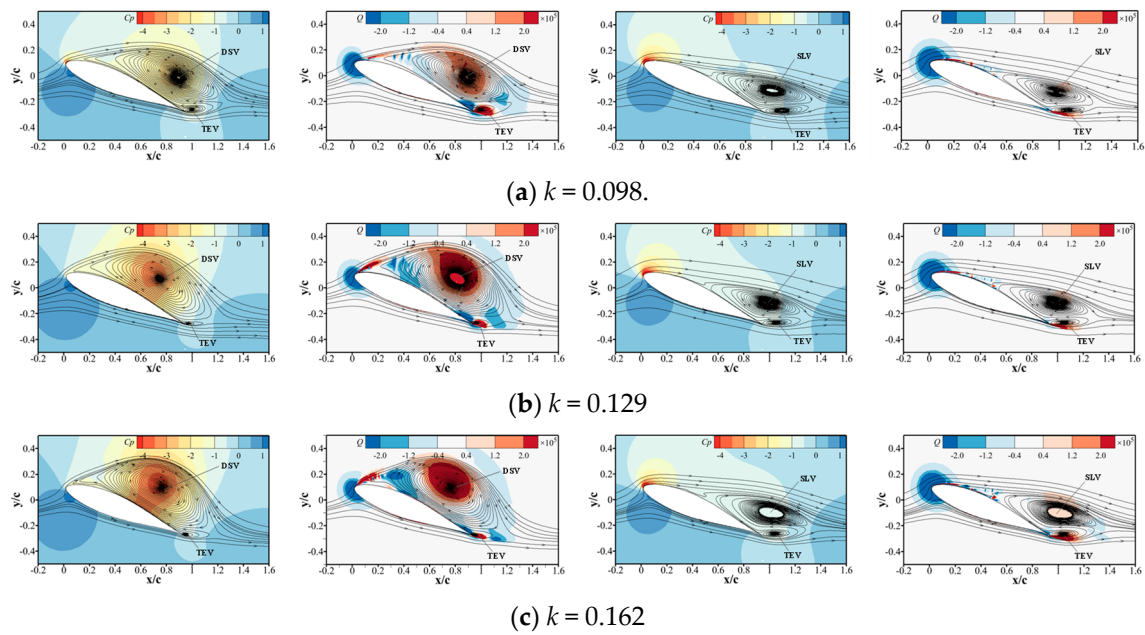


**Figure 17.**  $C_p$  contour and  $Q$  contour of the airfoil under different reduced frequencies (baseline is in left column and controlled in right).

## 6. Conclusions

Based on motion-nested grid technology, the SST  $k-\omega$  turbulence model was used to numerically simulate the flow field characteristics of the NACA63-218 airfoil dynamic stall by solving the unsteady Reynolds-averaged Navier–Stokes equation. Based on the spatiotemporal evolution characteristics of the flow field structure and wall pressure distribution, the evolution process of the dynamic stall vortex structure and the primary controlling vortex mechanism influencing the nonlinear aerodynamic effects were revealed. In addressing the suppression of dynamic stall in airfoil behavior, the concept of distributed blowing flow control was introduced. The study explored the control effectiveness of distributed blowing positions and blowing coefficients in dynamic stall, as well as the dynamic stall suppression effect of distributed blowing control under various operating conditions. The conclusions were as follows:

- (1) The evolution and motion characteristics of the DSV and SLV during dynamic stall led to nonlinear hysteresis in the aerodynamics. In the upstroke process, separation first occurred at the trailing edge, forming the SLV. As the angle of attack gradually increased, vorticity accumulated at the leading edge of the airfoil, forming the LEV. With a further increase in the angle of attack, the LEV and the SLV rapidly merged, causing a vortex eruption. This vorticity convection was downstream, forming the DSV, resulting in a sudden spike in aerodynamic forces and pitch moment coefficients to their maximum values. In the downstroke process, the strength of the TEV increased, inducing low-energy fluid in the dissipation region of the DSV, forming the SDSV. This resulted in a secondary dynamic stall and the aerodynamic coefficients exhibited a secondary peak phenomenon, although with relatively smaller magnitudes.
- (2) To control the formation and merging of the SLV and DSV, the concept of distributed blowing control was introduced. The study investigated the control effectiveness of changes in the distributed blowing positions and blowing coefficients on the aerodynamics. The results indicated that distributed blowing control could suppress the formation of the DSV and reduce the intensity of the SLV, thereby lowering the aerodynamic peak values during dynamic stall. There existed an optimal blowing coefficient, and when the blowing coefficient  $C_\mu$  exceeded 0.03, the effectiveness of blowing control no longer significantly improved.

- (3) The control effectiveness of distributed blowing control on dynamic stall was investigated under various operating conditions. The results indicated that under different motion parameters, distributed blowing control could suppress the formation of the DSV, transforming the primary controlling vortex structure in the flow field into the SLV. When distributed blowing control was applied at the positions  $x/c = 5\%$ ,  $10\%$ , and  $30\%$  with a blowing momentum coefficient  $C_{\mu}$  of 0.0156, it reduced the peak values of the drag coefficient by 70% and the pitch moment coefficient by 72%, and decreased the hysteresis loop area of the lift coefficient by 46%. Moreover, near the maximum stall angle, distributed blowing control could mitigate stall characteristics, resulting in a smoother variation in unsteady loads.

**Author Contributions:** Conceptualization, G.L. and S.Y.; methodology, G.L.; software, B.L.; validation, G.L., B.L. and X.Z.; resources, G.L.; data curation, B.L.; writing—original draft preparation, G.L. and B.L.; writing—review and editing, G.L. and B.L.; project administration, G.L.; funding acquisition, G.L. All authors have read and agreed to the published version of the manuscript.

**Funding:** This work was supported by the pre research project, China Aerodynamics Research and Development Center (50906030601), and exploratory research project, China Aerodynamics Research and Development Center (JK20211A020092).

**Data Availability Statement:** Data are contained within the article.

**Conflicts of Interest:** The authors declare no conflicts of interest.

## References

- Leishman, G.J. *Principles of Helicopter Aerodynamics with CD Extra*; Cambridge University Press: Cambridge, UK, 2006; pp. 761–763.
- Mulleners, K.; Raffel, M. Dynamic stall development. *Exp. Fluids* **2013**, *54*, 1469. [[CrossRef](#)]
- Gardner, A.D.; Jones, A.R.; Mulleners, K.; Naughton, J.W.; Smith, M.J. Review of rotating wing dynamic stall: Experiments and flow control. *Prog. Aerosp. Sci.* **2023**, *137*, 100887. [[CrossRef](#)]
- Conlisk, A.T. Modern helicopter rotor aerodynamics. *Prog. Aerosp. Sci.* **2001**, *37*, 419–476. [[CrossRef](#)]
- Zi, K.A.N.; Daochun, L.I.; Tong, S.H.E.N.; Xiang, J.; Zhang, L. Aerodynamic characteristics of morphing wing with flexible leading-edge. *Chin. J. Aeronaut.* **2020**, *33*, 2610–2619.
- Corke, T.C.; Thomas, F.O. Dynamic Stall in Pitching Airfoil: Aerodynamic Damping and Compressibility Effects. *Annu. Rev. Fluid. Mech.* **2015**, *47*, 479–505. [[CrossRef](#)]
- Himmel, S.H. *Profile Investigations on a Rotating Production Airscrew*; Ministry of Aircraft: Gottingen, Germany, 1947; p. 832.
- Harri, F.D.; Pruyne, R.R. Blade Stall—Half Fact, Half Fiction. *J. Am. Helicopter Soc.* **1968**, *13*, 27–48. [[CrossRef](#)]
- McCroskey, W.J.; Carr, L.W.; McAlister, K.W. Dynamic Stall Experiments on Oscillating Airfoils. *AIAA J.* **1976**, *14*, 57–63. [[CrossRef](#)]
- Carr, L.W. Progress in analysis and prediction of dynamic stall. *J. Aircr.* **1988**, *25*, 6–17. [[CrossRef](#)]
- McAlister, K.W.; Carr, L.W.; McCroskey, W.J. *Dynamic Stall Experiments on the NACA 0012 Airfoil*; Technical Report No. NASA-TP-1100; NASA: Washington, DC, USA, 1978.
- Geissler, W.; Raffel, M.; Dietz, G.; Mai, H. Helicopter aerodynamics with emphasis placed on dynamic stall. In *Wind Energy: Proceedings of the Euromech Colloquium*; Springer: Berlin/Heidelberg, Germany, 2007; pp. 199–204.
- Wang, Q.; Zhao, Q.J. Experiments on unsteady vortex flow field of typical rotor airfoils under dynamic stall conditions. *Chin. J. Aeronaut.* **2016**, *29*, 358–374. [[CrossRef](#)]
- Ekaterinaris, J.A.; Platzer, M.F. Computational prediction of airfoil dynamic stall. *Prog. Aerosp. Sci.* **1997**, *33*, 759. [[CrossRef](#)]
- Naughton, J.; Strike, J.; Hind, M.; Magstadt, A.; Babbitt, A. Measurements of Dynamic Stall on the DU Wind Turbine Airfoil Series. In Proceedings of the 69th Annual Forum of the American Helicopter Society, Phoenix, AZ, USA, 21–23 May 2013.
- Ullah, A.H.; Fabijanic, C.; Refling, W.; Estevadeordal, J. A Lifetime-PSP Study of Dynamic Stall on Pitching Swept Finite-Aspect-Ratio Wings. In Proceedings of the AIAA SCITECH 2022 Forum, San Diego, CA, USA & Virtual, 3–7 January 2022. AIAA Paper No. 2022-1959.
- Gardner, A.D.; Klein, C.; Sachs, W.; Henne, U.; Mai, H.; Richter, K. Investigation of three-dimensional dynamic stall on an airfoil using fast-response pressure-sensitive paint. *Exp. Fluids* **2014**, *55*, 1807. [[CrossRef](#)]
- Disotell, K.J.; Nikoueeyan, P.; Naughton, J.W.; Gregory, J.W. Global surface pressure measurements of static and dynamic stall on a wind turbine airfoil at low Reynolds number. *Exp. Fluids* **2016**, *57*, 82. [[CrossRef](#)]
- Larsson, J.; Kawai, S.; Bodart, J.; Bermejo-Moreno, I. Large eddy simulation with modeled wall-stress: Recent progress and future directions. *Mech. Eng. Rev.* **2016**, *3*, 15–00418. [[CrossRef](#)]
- Khalifa, N.M.; Rezaei, A.S.; Taha, H.E. Comparing the performance of different turbulence models in predicting dynamic stall. In Proceedings of the AIAA Scitech 2021 Forum, Virtual Event, 11–15 & 19–21 January 2021. AIAA Paper No. 2021-1651.

21. Xu, Z.; Wu, B.; Gao, C.; Wang, N. Numerical simulation of dynamic stall flow control using a multi-dielectric barrier discharge plasma actuation strategy. *Phys. Plasmas* **2022**, *29*, 103503. [[CrossRef](#)]
22. Wang, S.; Ingham, D.B.; Ma, L.; Pourkashanian, M.; Tao, Z. Turbulence modeling of deep dynamic stall at relatively low Reynolds number. *J. Fluids Struct.* **2012**, *33*, 191–209. [[CrossRef](#)]
23. Kaufmann, K.; Costes, M.; Richez, F.; Gardner, A.D.; Pape, A.L. Numerical investigation of three-dimensional static and dynamic stall on a finite wing. *J. Am. Helicopter Soc.* **2015**, *60*, 1–12. [[CrossRef](#)]
24. Jain, R.; Le Pape, A.; Grubb, A.; Costes, M.; Richez, F.; Smith, M. High-Resolution Computational Fluid Dynamics Predictions for the Static and Dynamic Stall of a Finite-Span OA209 Wing. *J. Fluids Struct.* **2018**, *78*, 126–145. [[CrossRef](#)]
25. Costes, M.; Richez, F.; Le Pape, A.; Gaveriaux, R. Numerical Investigation of Three-Dimensional Effects During Dynamic Stall. In Proceedings of the 37th European Rotorcraft Forum, Gallarate, Italy, 13–15 September 2011.
26. Visbal, M.R.; Garmann, D.J. Dynamic stall of a finite aspect-ratio wing. *AIAA J.* **2019**, *57*, 962–977. [[CrossRef](#)]
27. Visbal, M.R.; Garmann, D.J. Effect of sweep on dynamic stall of a pitching finite-aspect-ratio wing. *AIAA J.* **2019**, *57*, 3274–3289. [[CrossRef](#)]
28. Visbal, M.R.; Garmann, D.J. Analysis of dynamic stall on a pitching airfoil using high-fidelity large-eddy simulations. *AIAA J.* **2018**, *56*, 46–63. [[CrossRef](#)]
29. Visbal, M.R.; Benton, S.I. Exploration of high-frequency control of dynamic stall using large-eddy simulations. *AIAA J.* **2018**, *56*, 2974–2991. [[CrossRef](#)]
30. Zhong, J.; Li, J.; Guo, P. Effects of leading-edge rod on dynamic stall performance of a wind turbine airfoil. *Proc. Inst. Mech. Eng. Part A* **2017**, *231*, 753–769. [[CrossRef](#)]
31. Niu, J.; Lei, J.; Lu, T. Numerical research on the effect of variable droop leading-edge on oscillating NACA 0012 airfoil dynamic stall. *Aerosp. Sci. Technol.* **2018**, *72*, 476–485. [[CrossRef](#)]
32. Zhao, G.Q.; Zhao, Q.J. Dynamic stall control optimization of rotor airfoil via variable droop leading-edge. *Aerosp. Sci. Technol.* **2015**, *43*, 406–414. [[CrossRef](#)]
33. Martin, P.; Mcalister, K.; Chandrasekhara, M.; Geissler, W. Dynamic Stall Measurements and Computations for a VR-12 Airfoil with a Variable Droop Leading Edge. In Proceedings of the American Helicopter 59th Annual Forum, Phoenix, AZ, USA, 6–8 May 2003.
34. Lorber, P.F.; Carta, F.O.; Covino, A.F., Jr. *An Oscillating Three-Dimensional Wing Experiment: Compressibility, Sweep, Rate, Waveform and Geometry Effects on Unsteady Separation and Dynamic Stall*. Report R92-958325-6; United Technologies Research Center: Farmington, NM, USA, 1992.
35. Raiola, M.; Discetti, S.; Ianiro, A.; Samara, F.; Avallone, F.; Ragni, D. Smart rotors: Dynamic-stall load control by means of an actuated flap. *AIAA J.* **2018**, *56*, 1388–1401. [[CrossRef](#)]
36. Zanotti, A.; Grassi, D.; Gibertini, G. Experimental investigation of a trailing edge L-shaped tab on a pitching airfoil in deep dynamic stall conditions. *Proc. Inst. Mech. Eng. Part. G J. Aerosp. Eng.* **2014**, *228*, 2371–2382. [[CrossRef](#)]
37. Samara, F.; Johnson, D.A. Dynamic stall on pitching cambered airfoil with phase offset trailing edge flap. *AIAA J.* **2020**, *58*, 2844–2856. [[CrossRef](#)]
38. Joo, W.; Lee, B.; Yee, K.; Lee, D.-H. Combining passive control method for dynamic stall control. *J. Aircr.* **2006**, *43*, 1120–1128. [[CrossRef](#)]
39. Lee, B.; Yee, K.; Joo, W.; Lee, D.-H. Dynamic Stall Control with Droop Leading Edge and Gurney Flap. *J. Korean Soc. Aeronaut. Space Sci.* **2004**, *32*, 10–17.
40. Chandrasekhara, M.S. Optimum gurney flap height determination for lost-lift recovery in compressible dynamic stall control. *Aerosp. Sci. Technol.* **2010**, *14*, 551–556. [[CrossRef](#)]
41. De Tavernier, D.; Ferreira, C.; Vire, A.; LeBlanc, B.; Bernardy, S. Controlling dynamic stall using vortex generators on a wind turbine airfoil. *Renew. Energy* **2021**, *172*, 1194–1211. [[CrossRef](#)]
42. Zhu, C.; Chen, J.; Wu, J.; Wang, T. Dynamic stall control of the wind turbine airfoil via single-row and double-row passive vortex generators. *Energy* **2019**, *189*, 116272. [[CrossRef](#)]
43. Green, R.B.; Prince, S.A.; Wang, Y.; Khodagolian, V.; Coton, F.N. Delay of dynamic stall using pulsed air-jet vortex generators. *AIAA J.* **2018**, *56*, 2070–2074. [[CrossRef](#)]
44. Liu, J.; Chen, R.; You, Y.; Shi, Z. Numerical investigation of dynamic stall suppression of rotor airfoil via improved co-flow jet. *Chin. J. Aeronaut.* **2022**, *35*, 169–184. [[CrossRef](#)]
45. Gardner, A.D.; Richter, K.; Mai, H.; Neuhaus, D. Experimental investigation of air jets to control shock-induced dynamic stall. *J. Am. Helicopter Soc.* **2014**, *59*, 1–11. [[CrossRef](#)]
46. Dano, B.; Zha, G.C.; Castillo, M. *Experimental Study of Co-Flow Jet Airfoil Performance Enhancement Using Discreet Jets*; Report No.: AIAA-2011-0941; AIAA: Reston, VA, USA, 2011.
47. Lefebvre, A.; Dano, B.; Bartow, W.B.; Difronzo, M.; Zha, G.C. Performance and energy expenditure of coflow jet airfoil with variation of Mach number. *J. Aircr.* **2016**, *53*, 1757–1767. [[CrossRef](#)]
48. Zhao, G.; Zhao, Q. Parametric analyses for synthetic jet control on separation and stall over rotor airfoil. *Chin. J. Aeronaut.* **2014**, *27*, 1051–1061. [[CrossRef](#)]
49. Kissing, J.; Stumpf, B.; Kriegseis, J.; Hussong, J.; Tropea, J. Delaying leading edge vortex detachment by plasma flow control at topologically critical locations. *Phys. Rev. Fluids* **2021**, *6*, 023101. [[CrossRef](#)]

50. Mukherjee, S.; Roy, S. Enhancement of lift and drag characteristics of an oscillating airfoil in deep dynamic stall using plasma actuation. In Proceedings of the 50th AIAA Aerospace Sciences Meeting Including the New Horizons Forum and Aerospace Exposition, Nashville, TN, USA, 9–12 January 2012. AIAA Paper No. 2012-702.
51. Li, G.; Yi, S. Large eddy simulation of dynamic stall flow control for wind turbine airfoil using plasma actuator. *Energy* **2020**, *212*, 118753.
52. Yu, H.; Zheng, J. Numerical investigation of control of dynamic stall over a NACA0015 airfoil using dielectric barrier discharge plasma actuators. *Phys. Fluids* **2020**, *32*, 035103. [[CrossRef](#)]
53. Yang, H.S.; Zhao, G.Y.; Liang, H.; Wei, B. Dynamic stall control over an airfoil by NS-DBD actuation. *Chin. Phys. B* **2020**, *29*, 105203. [[CrossRef](#)]
54. Ramesh, K.; Gopalarathnam, A.; Granlund, K.; Ol, M.V.; Edwards, J.R. Discrete-vortex method with novel shedding criterion for unsteady aerofoil flows with intermittent leading-edge vortex shedding. *J. Fluid. Mech.* **2014**, *751*, 500. [[CrossRef](#)]
55. Ma, Y.Y.; Zhao, Q.J.; Zhao, G.Q. New combinational active control strategy for improving aerodynamic characteristics of airfoil and rotor. *Proc. Inst. Mech. Eng. Part. G J. Aerosp. Eng.* **2020**, *234*, 977–996. [[CrossRef](#)]
56. Visbal, M.R.; Garmann, D.J. Investigation of spanwise end effects on dynamic stall of a pitching wing section. *J. Aircr.* **2019**, *56*, 2118–2130. [[CrossRef](#)]
57. Gardner, A.D.; Richter, K.; Rosemann, H. Numerical investigation of air jets for dynamic stall control on the OA209 airfoil. *CEAS Aeronaut. J.* **2011**, *1*, 69–82. [[CrossRef](#)]
58. Lind, A.H. An Experimental Study of Static and Oscillating Rotor Blade Sections in Reverse Flow. Ph.D. Thesis, University of Maryland, College Park, MD, USA, 2015; pp. 5–10.
59. Khalifa, N.M.; Rezaei, A.; Taha, H.E. On computational simulations of dynamic stall and its three-dimensional nature. *Phys. Fluids* **2023**, *35*, 105143. [[CrossRef](#)]
60. Carta, M.; Putzu, R.; Ghisu, T. A comparison of plunging- and pitching-induced deep dynamic stall on an SD7003 airfoil using URANS and LES simulations. *Aerosp. Sci. Technol.* **2022**, *121*, 107307. [[CrossRef](#)]
61. Bertagnolio, F.; Johansen, J.; Uglsang, P. *Wind Turbine Airfoil Catalogue*; Risø National Laboratory: Roskilde, Denmark, 2001; pp. 13–16.
62. Jing, S.; Zhao, G.; Zhao, Q. Numerical research on secondary peak of aerodynamic forces of airfoil under dynamic stall. *J. Nanjing Univ. Aeronaut. Astronaut.* **2022**, *54*, 191–202.

**Disclaimer/Publisher’s Note:** The statements, opinions and data contained in all publications are solely those of the individual author(s) and contributor(s) and not of MDPI and/or the editor(s). MDPI and/or the editor(s) disclaim responsibility for any injury to people or property resulting from any ideas, methods, instructions or products referred to in the content.